Potential Poroelastic Triggering of the 2020 M5.0 Mentone Earthquake in the Delaware Basin, Texas, by Shallow Injection Wells

Xinyu Tan[1,1] and Semechah K. Y. Lui[2,2]

[1]University of Toronto - Mississauga
[2]University of Toronto

July 11, 2023

Abstract

The Delaware Basin in Texas, one of the largest oil and gas production sites in the US, has been impacted by widespread seismicity in recent years. The M5.0 earthquake that occurred in March 2020 near the town of Mentone is one of the largest induced earthquakes recorded in this region. Characterizing the source parameters and triggering mechanism of this major event is imperative to assess and mitigate future hazard risk. A former study showed that this event may be attributed to the deep injection nearby. Interestingly, the earthquake is located in proximity to shallow injection wells with much larger total injection volume. In this study, we investigate the role of these shallow injection wells in the triggering of the M5.0 event despite their farther distance from the mainshock. We perform source-parameter inversion and earthquake relocation to determine the precise orientation of the south-facing normal fault plane where the mainshock occurred, followed by fully coupled poroelastic stress modeling of the change of Coulomb Failure Stress (ΔCFS) on the fitted fault plane caused by shallow injection in the region. Results show that shallow wells caused up to 20 kPa of ΔCFS near the mainshock location, dominated by positive poroelastic stress change. Such perturbation surpasses the general triggering threshold of faults that are well aligned with the local stress field and suggests the nonnegligible role of these shallow wells in the triggering of the mainshock. We also discuss the complex effect of poroelastic stress perturbation in the subsurface and highlight the importance of detailed geomechanical evaluation of the reservoir when developing relevant operational and safety policies.

Potential Poroelastic Triggering of the 2020 M5.0 Mentone Earthquake in the Delaware Basin, Texas, by Shallow Injection Wells

Supplemental Material

by Xinyu Tan and Semechah K. Y. Lui

Contents of this file

Figures S1 to S15

Tables S1 to S10

Video S1

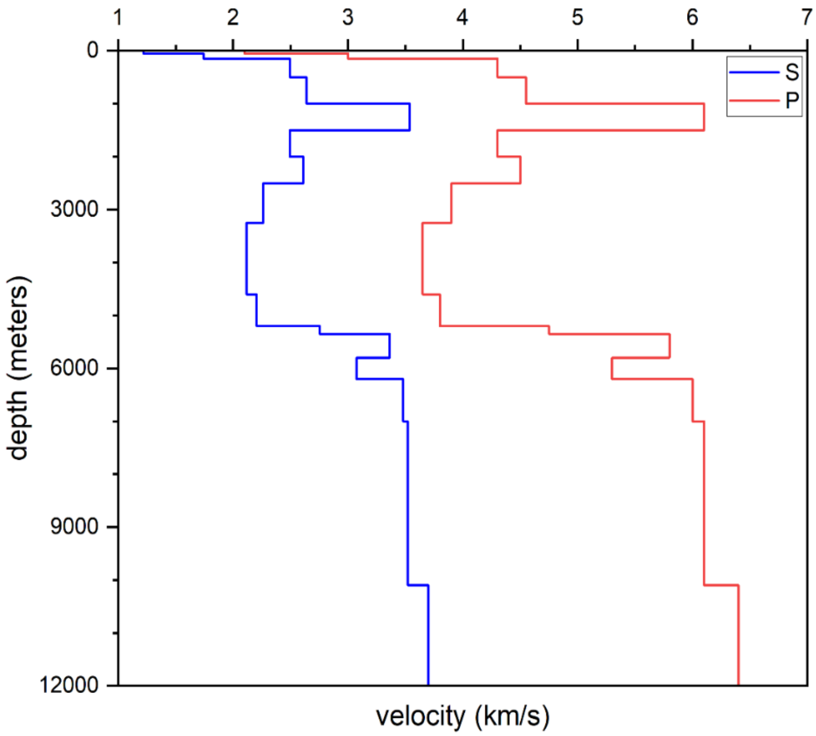

Figure S1. Velocity model used in CAP inversion (modified from Sheng et al., 2022).

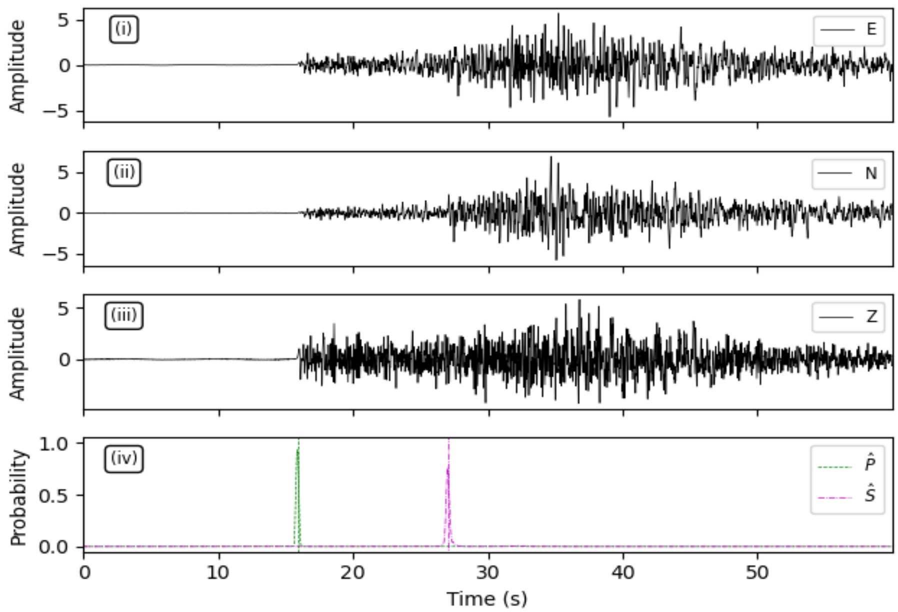

Figure S2. Example of phase pick output from PhaseNet.

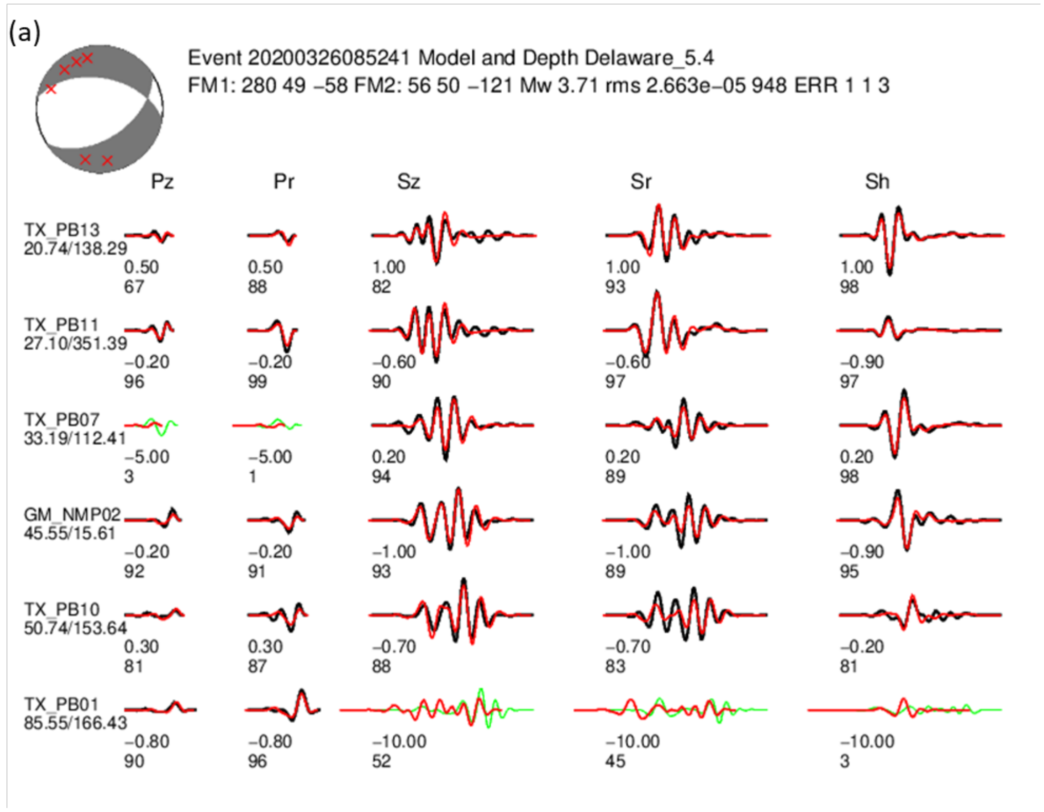

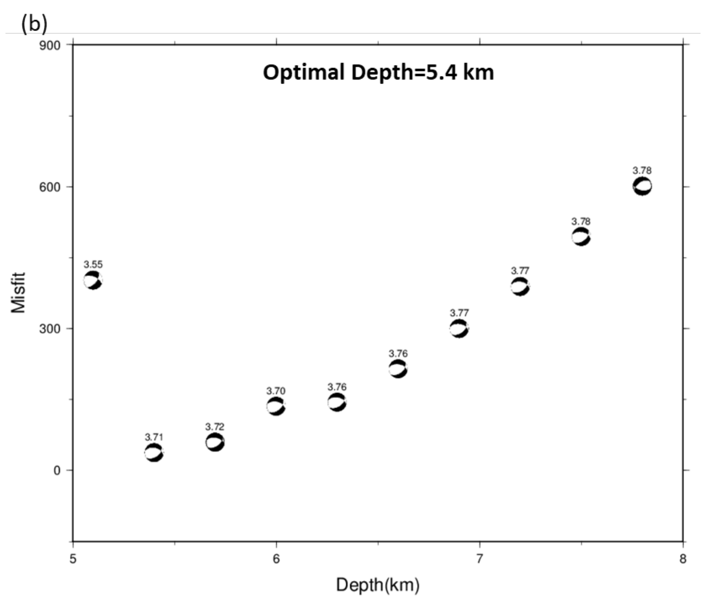

Figure S3. (a) Cross correlation (cc) of synthetic (red) and actual (black) waveforms at the optimal depth of event 02. Green waveforms are below the cc threshold and not accounted for in inversion results. The numbers below the waveforms are optimal shift time (in second) and cross correlation, respectively. (b) Relative misfit error of event 02 inversion at different focal depths.

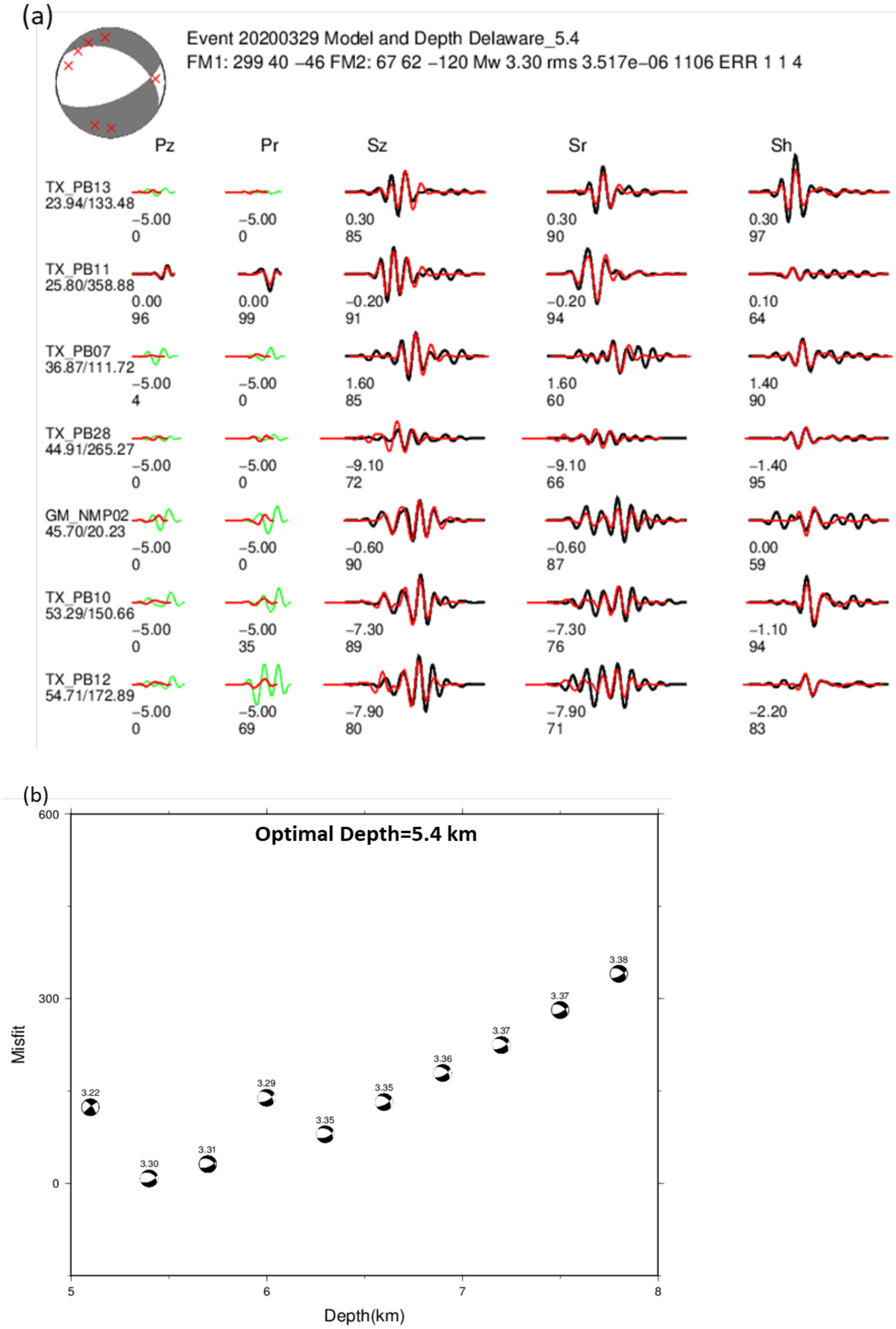

Figure S4. (a) Cross correlation (cc) of synthetic (red) and actual (black) waveforms at the optimal depth of event 03. Green waveforms are below the cc threshold and not accounted for in inversion results. The numbers below the waveforms are optimal shift time (in second) and cross correlation, respectively. (b) Relative misfit error of event 03 inversion at different focal depths.

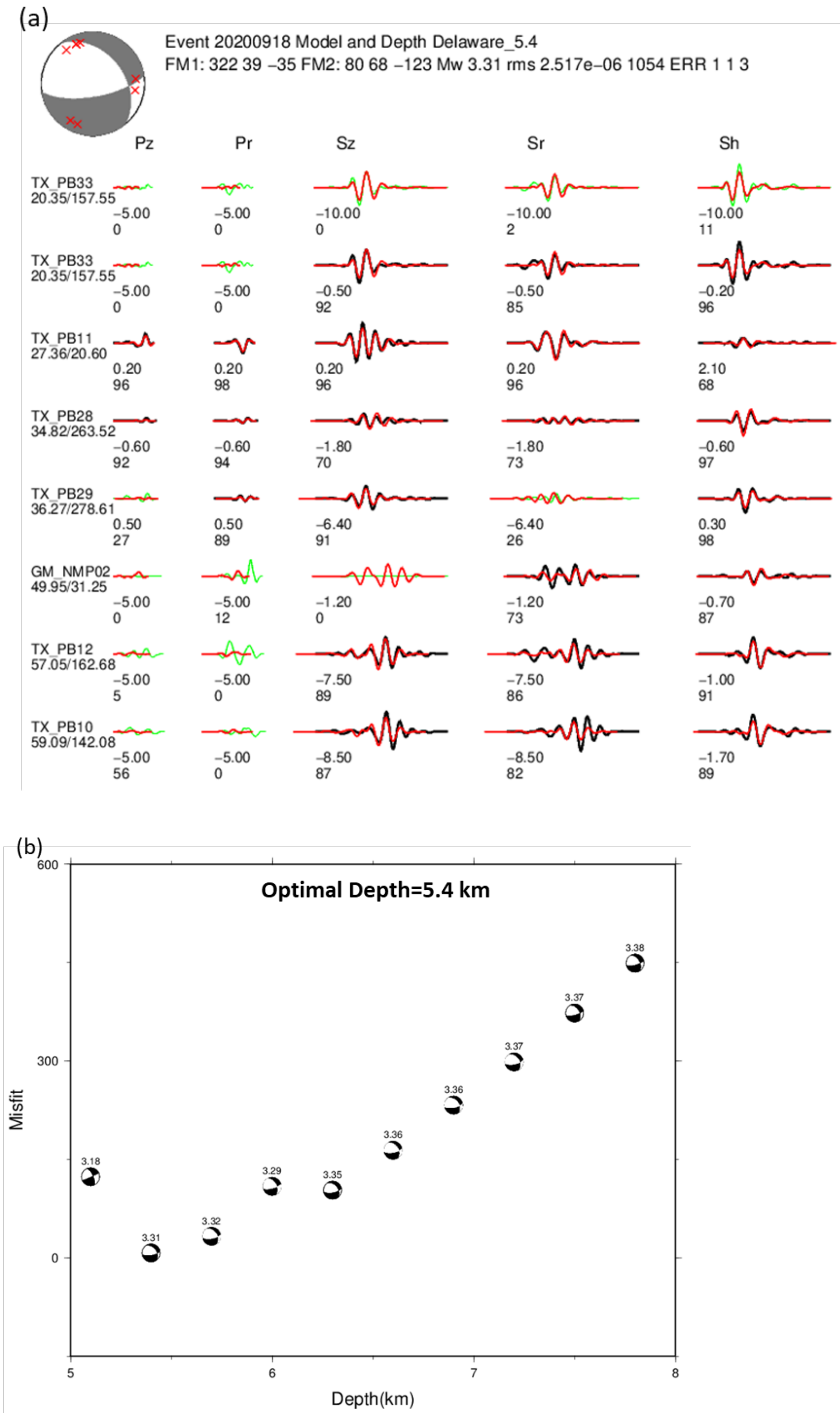

Figure S5. (a) Cross correlation (cc) of synthetic (red) and actual (black) waveforms at the optimal depth of event 04. Green waveforms are below the cc threshold and not accounted for in inversion results. The numbers below the waveforms are optimal shift time (in second) and cross correlation, respectively. (b) Relative misfit error of event 04 inversion at different focal depths.

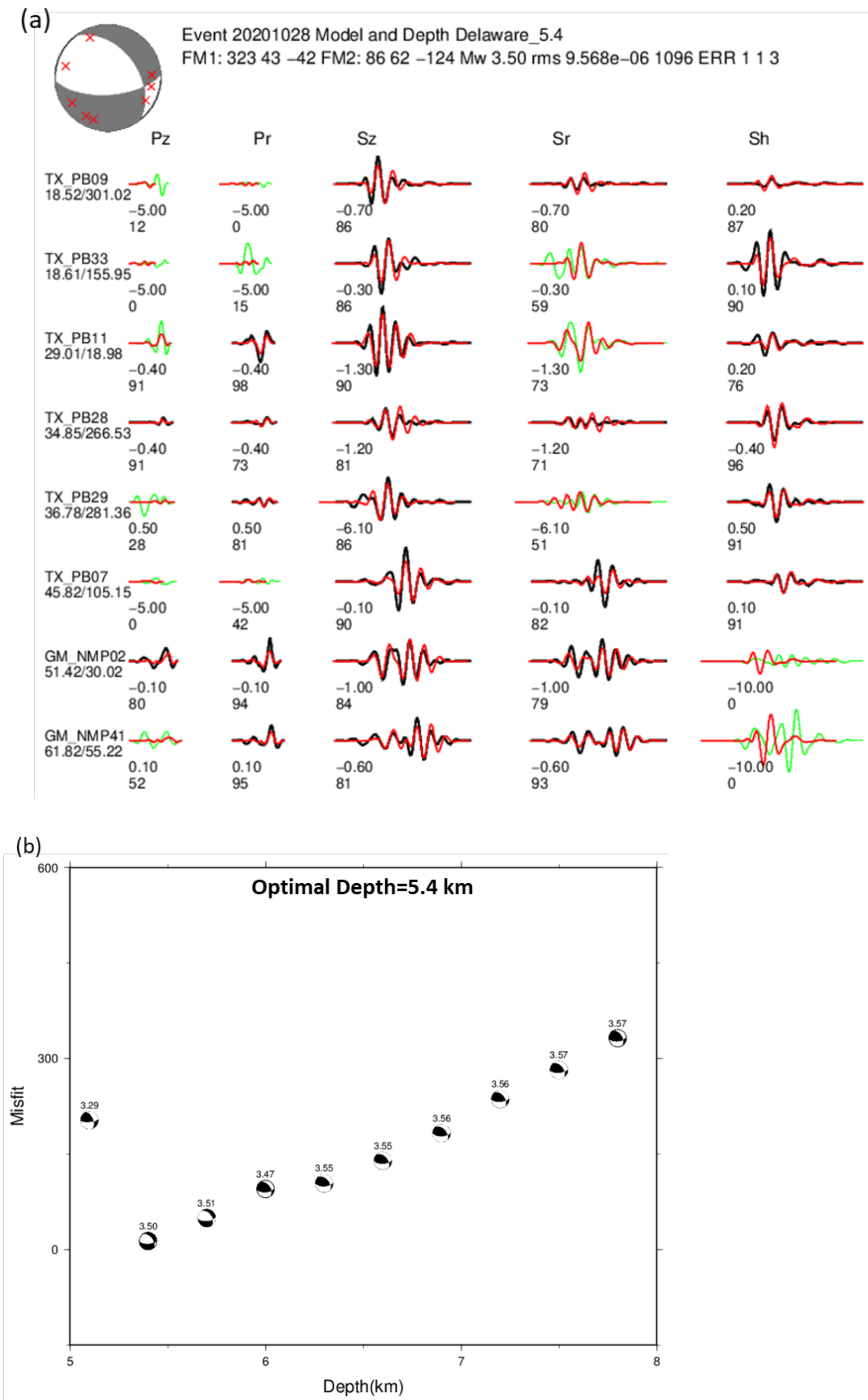

Figure S6. (a) Cross correlation (cc) of synthetic (red) and actual (black) waveforms at the optimal depth of event 05. Green waveforms are below the cc threshold and not accounted for in inversion results. The numbers below the waveforms are optimal shift time (in second) and cross correlation, respectively. (b) Relative misfit error of event 05 inversion at different focal depths.

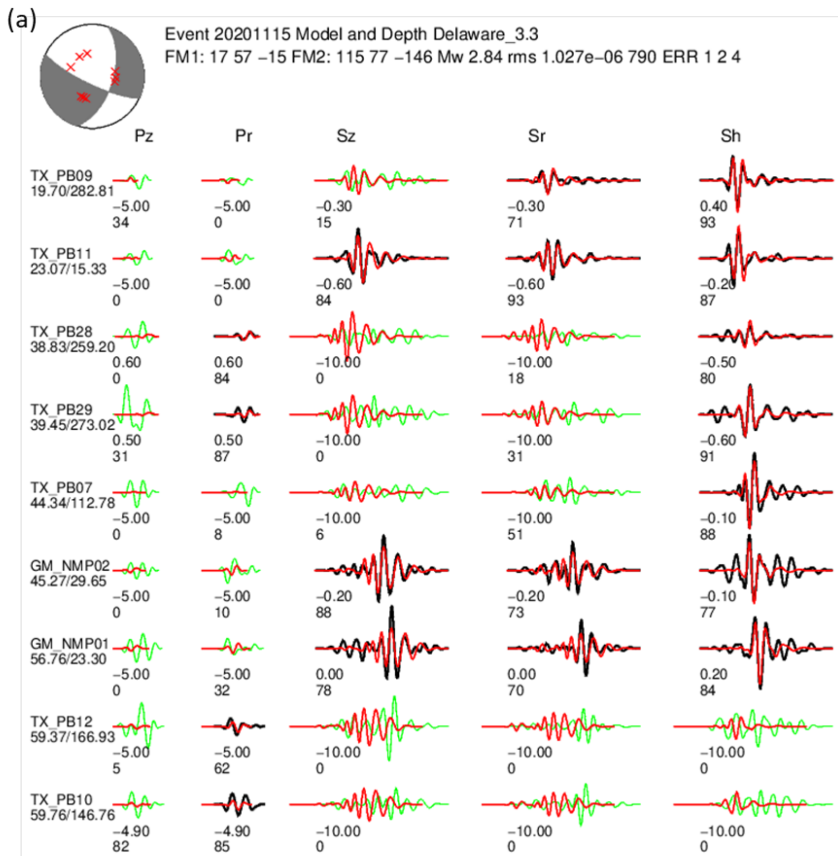

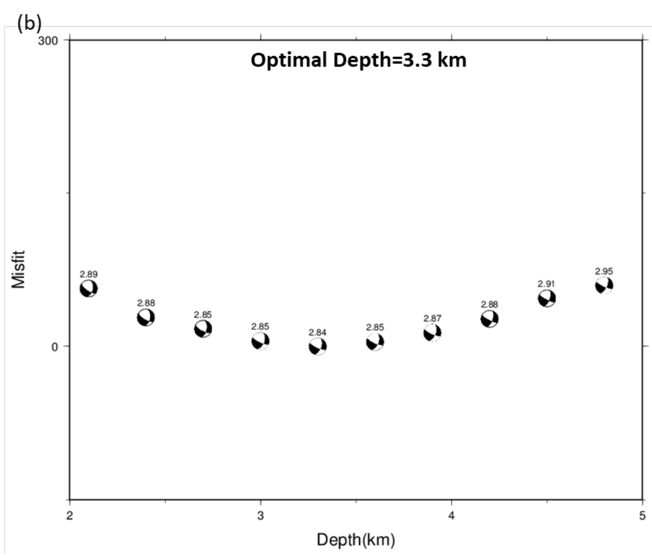

Figure S7. (a) Cross correlation (cc) of synthetic (red) and actual (black) waveforms at the optimal depth of event 06. Green waveforms are below the cc threshold and not accounted for in inversion results. The numbers below the waveforms are optimal shift time (in second) and cross correlation, respectively. (b) Relative misfit error of event 06 inversion at different focal depths.

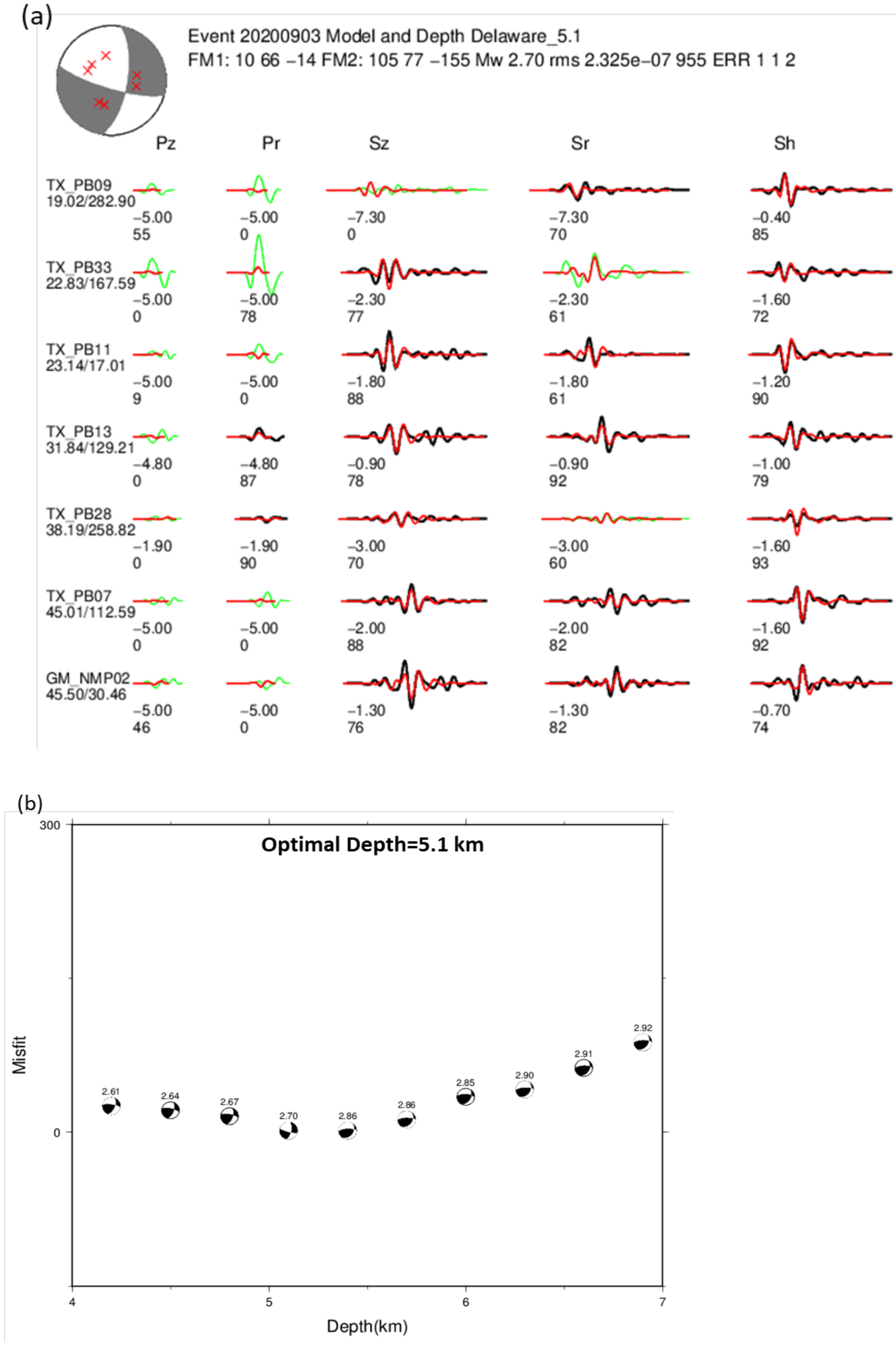

Figure S8. (a) Cross correlation (cc) of synthetic (red) and actual (black) waveforms at the optimal depth of event 07. Green waveforms are below the cc threshold and not accounted for in inversion results. The numbers below the waveforms are optimal shift time (in second) and cross correlation, respectively. (b) Relative misfit error of event 07 inversion at different focal depths.

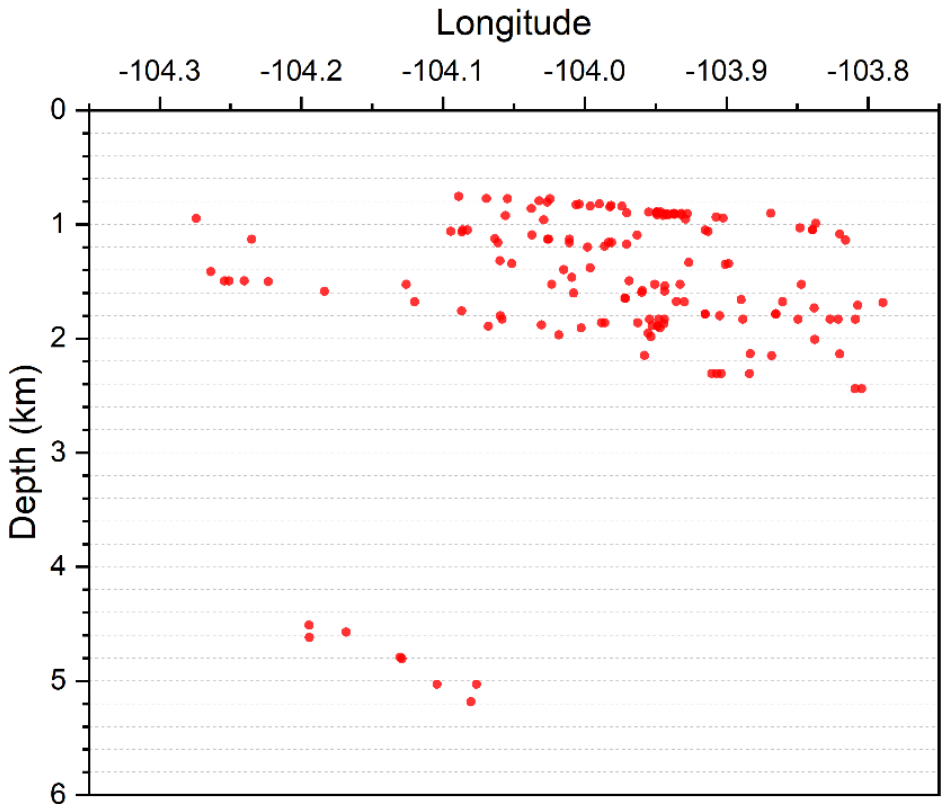

Figure S9. Distribution of well bottom depth.

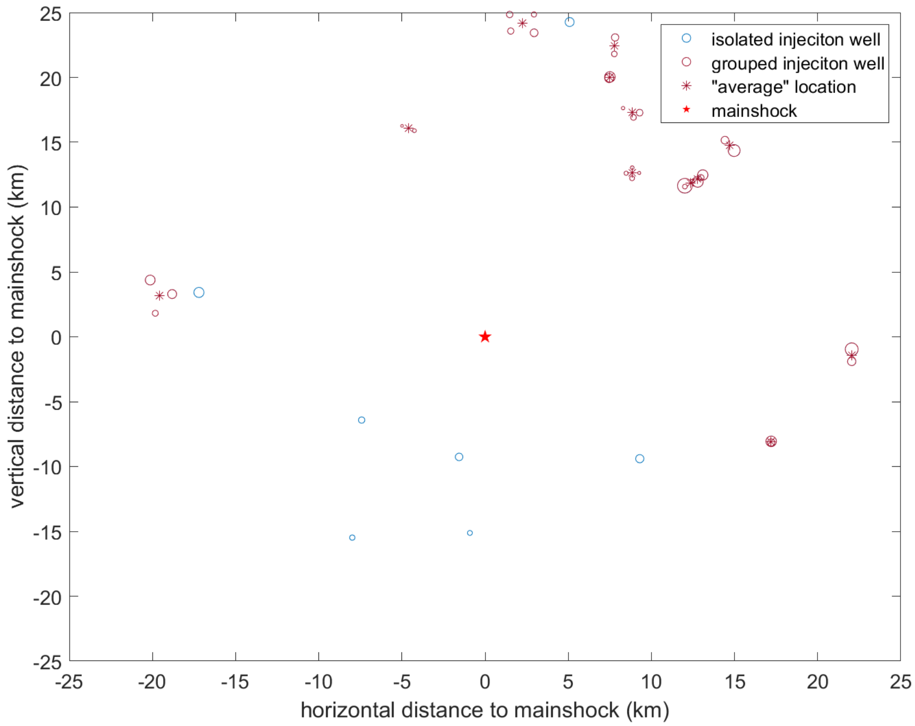

Figure S10. Distribution of injection wells and the averaged location of selected wells. Blue and brown circles represent isolated and grouped injection wells, respectively. The size of the circle is proportional to the total injection volume of injection wells. Brown asterisks indicate the averaged well locations. The red star is the mainshock location.

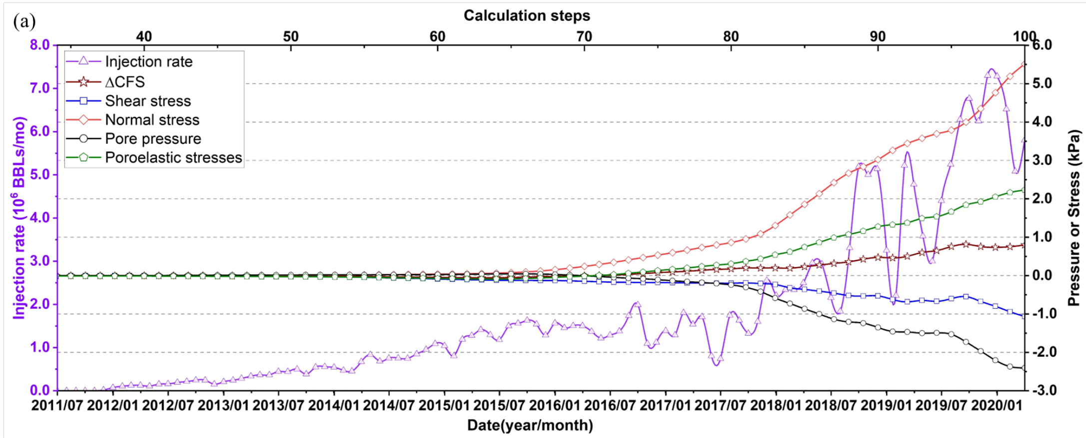
(a)
Calculation steps
Injection rate
ΔCFS
Shear stress
Normal stress
Pore pressure
Poroelastic stresses
Injection rate (10^6 BBLs/mo)
Pressure or Stress (kPa)
Date(year/month)

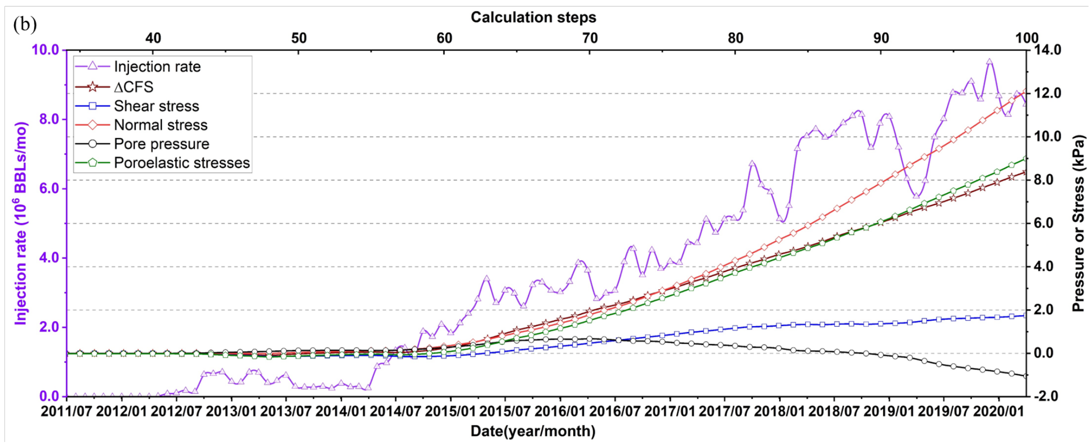
(b)
Calculation steps
Injection rate
ΔCFS
Shear stress
Normal stress
Pore pressure
Poroelastic stresses
Injection rate (10^6 BBLs/mo)
Pressure or Stress (kPa)
Date(year/month)

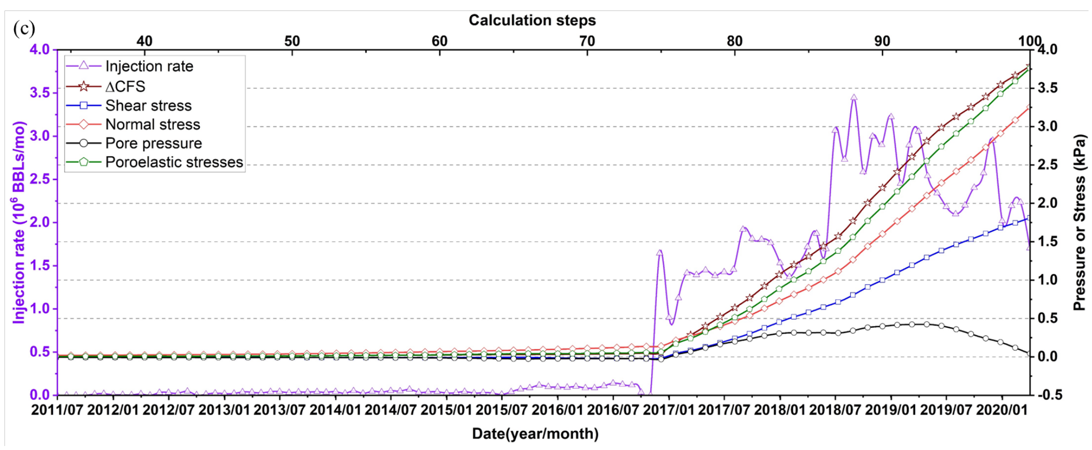
(c)
Calculation steps
Injection rate
ΔCFS
Shear stress
Normal stress
Pore pressure
Poroelastic stresses
Injection rate (10^6 BBLs/mo)
Pressure or Stress (kPa)
Date(year/month)

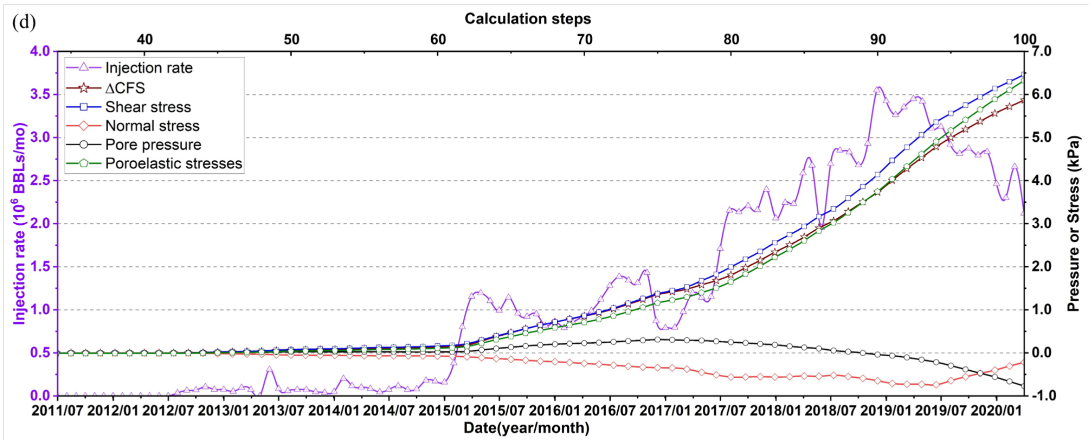

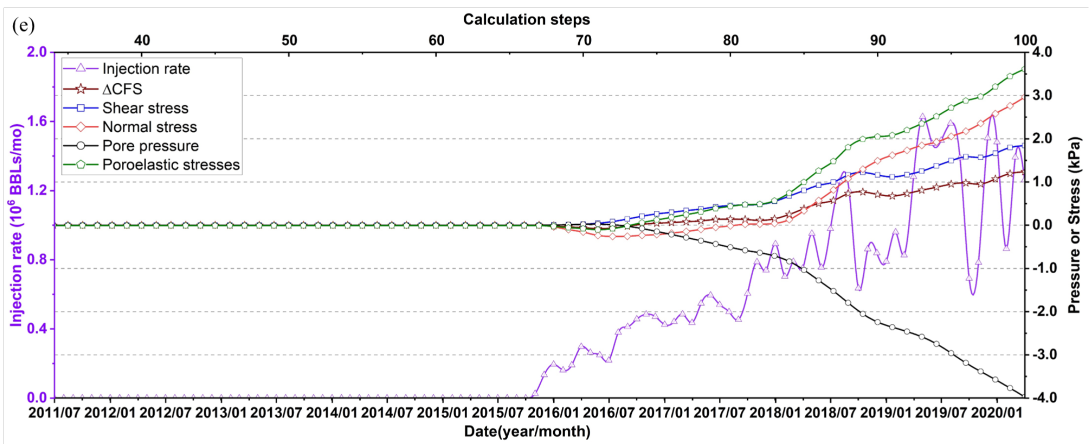

Figure S11. Time evolution of the monthly injection rate of selected deep (a) and shallow (b, c, d, and e corresponds to the northeast, northwest, southeast and southwest quadrants to the M5.0 event) injection wells, as well as the change in pore pressure, poroelastic stress, normal stress, shear stress and ΔCFS on the fitted fault plane near the mainshock location until the occurrence of the M5.0 mainshock.

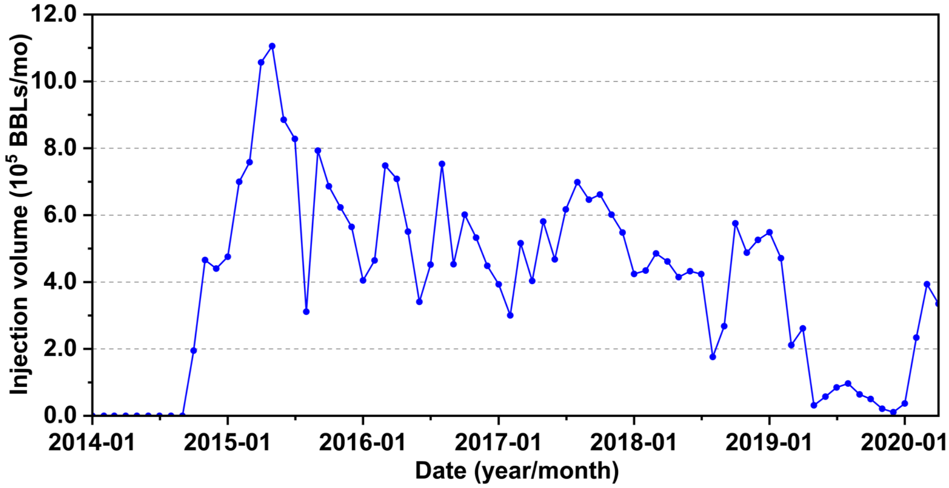

Figure S12. Monthly injection rate of selected shallow injection well (This well has no injection activity prior to January 2014).

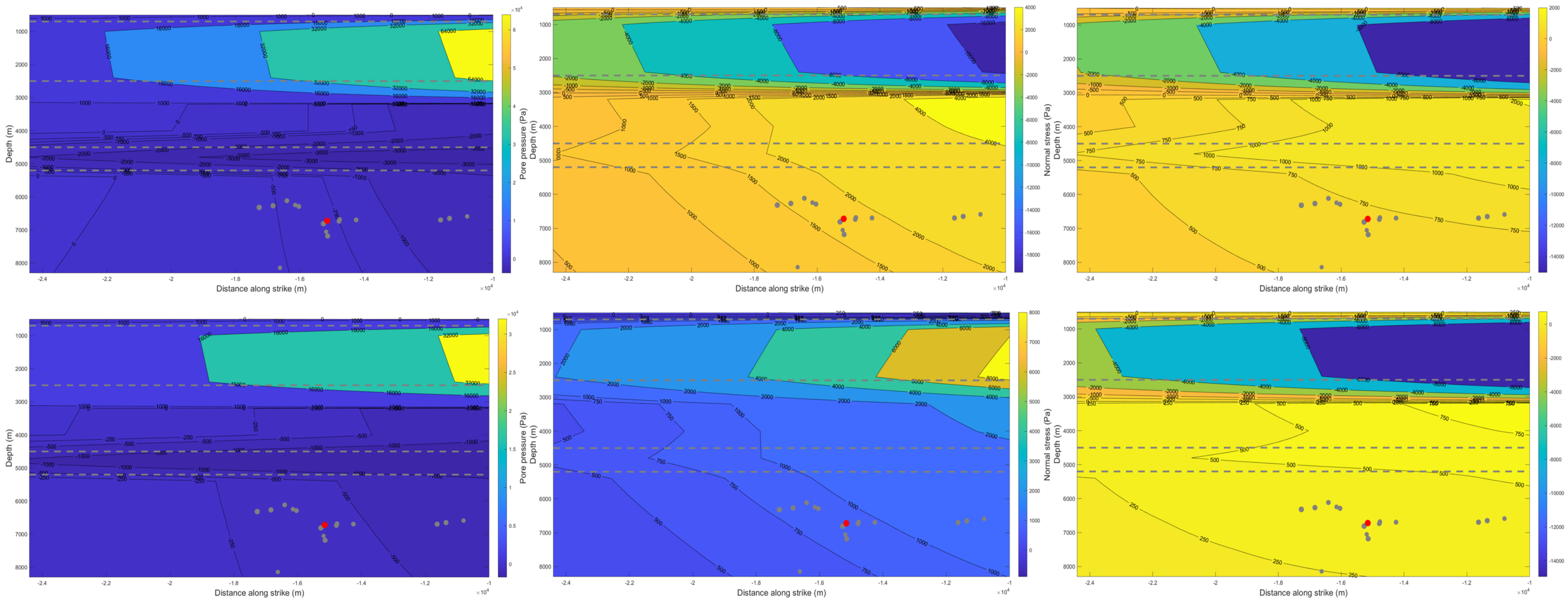

Figure S13. Resulted pore pressure, normal stress and shear stress of injection scenarios SI-1 and SI-2 (Top row: injection scenario SI-1, bottom row: injection scenario SI-2. From left to right: Pore pressure, normal stress, shear stress). Gray dashed lines separate the anhydrite/halite, sandstone, shale, limestone and basement layers (from top to bottom).

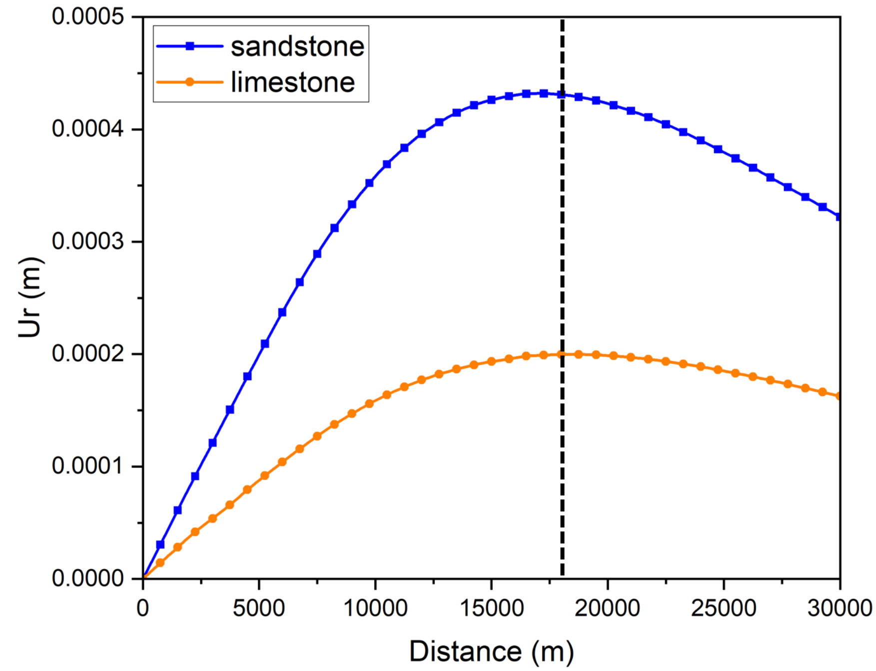

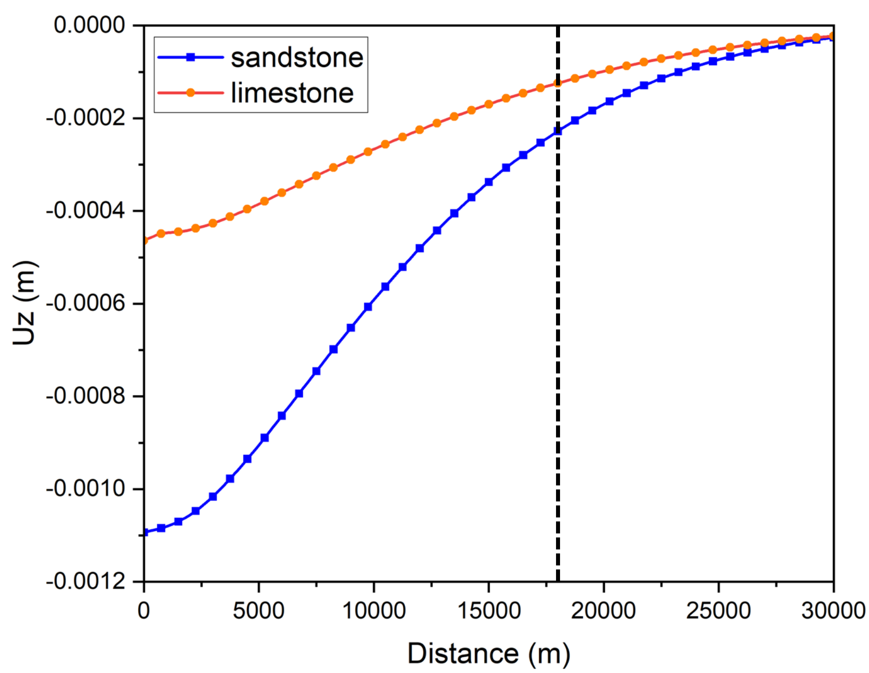

Figure S14. Simulated poroelastic deformation in the r and z direction within the basement layer where the mainshock occurred (depth = 6.7 km) as a result of shallow injections in scenario SI-1 (sandstone layer) and SI-2 (limestone layer), respectively. Here the injection is assumed to occur at distance = 0 m, and the dashed line indicates the mainshock location (a lateral distance of about 18 km from the injection source).

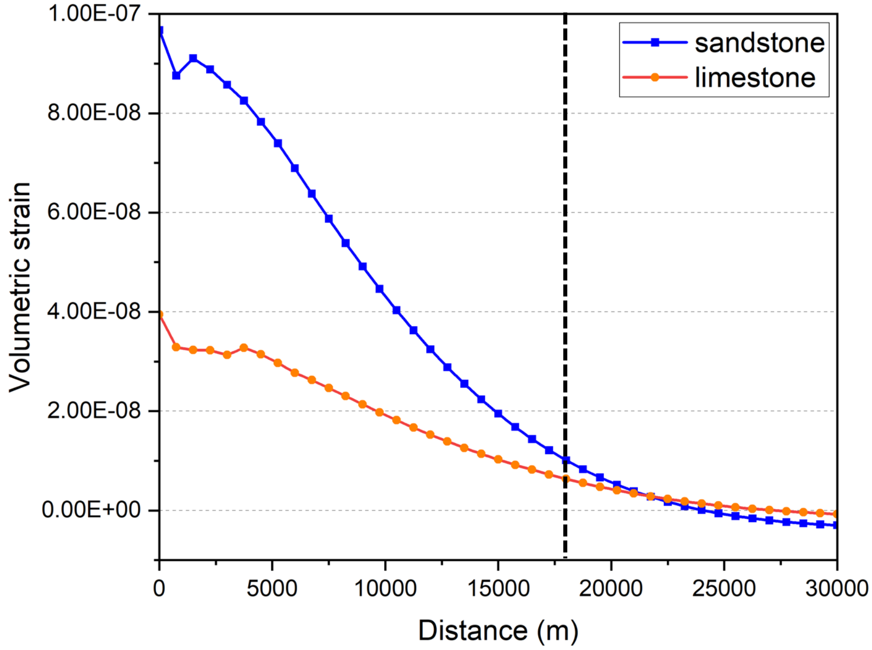

Figure S15. Resulted volumetric strain within the basement layer (at depth of 6.7 km) versus lateral distance from injection source in scenarios SI-1 (sandstone layer) and SI-2 (limestone layer). Here the injection is assumed to occur at distance = 0 m, and the dashed line indicates the mainshock location (a lateral distance of about 18 km from the injection source).

Table S1. Information of seismic stations used in earthquake relocation.

Station name	Latitude	Longitude	Distance to mainshock (km)
TXMB01	31.6677	-102.0829	185.80
TXMB02	31.1981	-102.0379	198.96
TXMB04	32.6254	-102.488	177.85
TXMB05	32.6265	-101.8597	229.20
TXMB06	31.978	-101.8	214.16
TXMB07	32.0006	-102.2528	172.21
TXPB01	30.9437	-103.7811	89.24
TXPB03	31.0838	-103.5139	86.30
TXPB04	31.187	-103.2693	94.04
TXPB05	30.9199	-103.3248	111.65
TXPB06	31.6472	-103.2182	78.48
TXPB07	31.5794	-103.6679	38.61
TXPB08	30.8917	-102.9074	141.54
TXPB09	31.7741	-104.3014	25.40
TXPB10	31.2836	-103.7546	55.25
TXPB11	31.9355	-104.0341	24.26
TXPB12	31.2132	-103.9577	56.41
TXPB13	31.5542	-103.8459	25.90
TXPB14	31.1293	-103.1511	106.85
TXPB15	31.2114	-103.0844	106.87
TXPB16	31.125	-103.252	99.73
TXPB17	30.9968	-103.1518	116.38
TXPB18	31.2008	-103.1996	98.40
TXPB19	31.3031	-103.0997	100.57
TXPB21	31.3419	-103.0622	101.91
TXPB27	31.5763	-103.1307	87.82
TXPB28	31.6686	-104.5008	43.83
TXPB29	31.753	-104.5145	44.96
TXPB30	31.2804	-103.3227	83.72
USMNTX	31.6985	-105.3821	127.06
4TNM01	32.3551	-103.3985	93.29
4TNM02	32.2641	-103.879	62.61
4TNM03	32.4726	-103.6343	92.22

SCPDB	32.0722	-103.5966	57.69
GMNMP01	32.2048	-103.8605	56.76
TXVHRN	30.7866	-104.9852	136.78
TXALPN	30.3745	-103.6385	153.72
SCJAL	32.2024	-103.2293	93.81
GMNMP02	32.0895	-103.8614	44.71
TXPCOS	31.4089	-103.5102	60.94
TXODSA	32.1201	-102.5491	148.10

Table S2. Input parameters used in hypoDD. (MINWGHT: minimum pick weight allowed, MAXDIST: maximum distance in km between event pair and stations, MAXSEP: maximum hypocentral separation in km, MAXNGH: maximum number of neighbors per event, MINLINK: minimum number of links required to define a neighbor, MINOBS: minimum number of links per pair saved, MAXOBS: maximum number of links per pair saved, NITER: number of iterations used for listed weights, WTCCP and WTCCS: weight of cross P wave and S wave, WRCC and WRCT: residual threshold in seconds for cross and catalog data, WTCTP and WTCTS: weight of catalog P wave and S wave, WDCC and WDCT: maximum distance (km) between cross and catalog linked pairs, DAMP: damping parameters used in iteration.

MINWGHT	MAXDIST	MAXSEP	MAXNGH	MINLINK	MINOBS	MAXOBS
0	400	6	8	8	1	50

NITER	WTCCP	WTCCS	WRCC	WDCC	WTCTP	WTCTS	WRCT	WDCT	DAMP
5	0.01	0.01	-9	-9	1.0	0.5	-9	-9	40
5	1	0.5	-9	6	0.001	0.001	-9	5	40
5	1	0.5	-9	5	0.001	0.001	6	5	40
5	1	0.5	6	5	0.001	0.001	6	5	40
5	1	0.5	6	3	0.001	0.001	6	3	40

Table S3. Results of jackknife resampling performed on clusters I, II and III and their uncertainty estimations.

fault-I 16 events		fault-II 8 events		fault-III 12 events	
strike	81	strike	95	strike	113
dip	52	dip	58	dip	73
Jackknife sampling 1000 times					
std(strike)	1.01	std(strike)	3.72	std(strike)	10.01
std(strike)/81	1.25%	std(strike)/95	3.91%	std(strike)/113	8.86%
std(dip)	6.41	std(dip)	8.57	std(dip)	18.63
std(dip)/52	12.33%	std(dip)/58	14.77%	std(dip)/73	25.52%
Jackknife sampling 2000 times					
std(strike)	0.99	std(strike)	3.78	std(strike)	9.82
std(strike)/81	1.22%	std(strike)/95	3.98%	std(strike)/113	8.69%
std(dip)	6.34	std(dip)	8.71	std(dip)	18.26
std(dip)/52	12.19%	std(dip)/58	15.02%	std(dip)/73	25.01%
Jackknife sampling 3000 times					
std(strike)	1.06	std(strike)	3.74	std(strike)	9.86
std(strike)/81	1.30%	std(strike)/95	3.94%	std(strike)/113	8.73%
std(dip)	6.74	std(dip)	8.59	std(dip)	18.32
std(dip)/52	12.96%	std(dip)/58	14.81%	std(dip)/73	25.09%

Table S4. Information of selected wells and resulted pore pressure, normal stress, shear stress and ΔCFS from POEL modeling. (Total injection volume is from January 2007 to March 2020).

Calculation groups	API number	Injection depth (m)	Total injection (BBLs)	Pore pressure (Pa)	Normal stress (Pa)	Shear stress (Pa)	ΔCFS (Pa)
NW_1_1	10932849	1499.9	26262354	-242.3	1296.9	679.0	1311.8
NW_1_2	10932848	1493.5	25035604	15.5	856.2	504.4	1027.4
NW_1_2	10933282	1493.5	20785411	224.6	570.8	445.0	922.3
NW_1_2	10933281	1493.5	9331550	157.8	226.6	187.7	418.3
NW_2	10931638	1064.4	4004484	-80.9	201.3	3.0	75.3
NW_2	10931565	1057.7	2063288	-31.1	104.1	-7.2	36.6
SE_1	38934609	2438.4	42808426	67.6	301.0	1760.2	1981.4
SE_1	38935413	2438.4	17916180	159.9	8.8	817.8	919.0
SE_2	38933269	1676.4	29133703	-195.0	-174.6	1470.7	1248.9
SE_2	38936297	1729.7	14006303	189.9	-468.5	905.9	738.8
SE_3	38935362	1582.8	17475621	-991.5	114.9	1509.9	983.9
SW_1	10933058	1828.8	14768626	-2416.7	2107.9	1022.2	836.9
SW_2	10932340	1676.4	10615573	-1257.3	1375.2	605.0	675.8
SW_3	10933071	1524.0	7493206	9.3	-522.2	57.4	-250.4
SW_4	38934925	1341.1	6382062	-307.2	3.4	157.9	-24.4
NE_1_1	38934274	1783.1	56124718	-710.7	2867.3	1319.8	2613.8
NE_1_1	38934372	1783.1	5884046	-136.5	314.1	121.4	227.9
NE_1_1	38933271	1798.3	9924847	-288.0	584.4	212.4	390.3
NE_1_2	38934237	2304.3	30472454	-693.9	1717.8	695.0	1309.3
NE_1_2	38934942	2304.3	27914073	-183.6	1370.6	708.7	1420.8
NE_1_2	38934935	2304.3	3625343	-26.6	182.8	86.8	180.6
NE_2	38934929	2304.3	36359171	153.1	1083.0	418.8	1160.4
NE_2	38935968	1656.9	15547400	254.5	346.4	125.0	485.6
NE_3	38934661	1859.3	29089012	100.2	640.1	-301.2	143.0
NE_3	38935357	1091.2	21147125	219.1	334.6	-316.8	15.4
NE_4	38933299	1127.8	15751034	30.5	213.4	-220.8	-74.5
NE_4	38935108	1158.2	7248901	80.7	16.5	-161.8	-103.5
NE_4	38933620	1127.8	10914961	41.8	118.3	-175.9	-79.8
NE_4	38933298	1127.8	10573269	-30.4	207.3	-97.9	8.2
NE_5	38932872	1828.8	11751801	-175.2	494.4	65.2	256.7

NE_5	38936030	1828.8	8596403	81.6	222.9	-38.0	144.6
NE_5	38936032	1828.8	3146446	77.9	51.7	-66.5	11.3
NE_6	38935886	1578.9	14115239	235.6	32.5	-345.3	-184.5
NE_6	38936478	1592.3	8264986	148.0	-2.0	-234.1	-146.6
NE_7	38935373	1859.3	20599155	231.1	73.7	-427.0	-244.1
NE_8	38932527	1889.2	6148354	-181.2	456.7	135.5	300.8
NE_8	38932506	1884.9	4547952	-113.6	324.9	101.3	228.1
NE_8	38932507	1887.6	3713541	-81.2	261.4	85.0	193.1
NE_8	38932528	1866.3	2602393	-87.3	201.7	59.0	127.7

Table S5. Information of injection wells: The averaged locations for various well groups, and true well locations for individual wells. Locations in bold are those used in the POEL model.

Calculation groups	API	Latitude	Longitude	Distance to average location (km)
NE_1_1_Average	N/A	**31.82351494**	**-103.9117379**	
NE_1_1	38934274	31.82183915	-103.9151514	0.37
NE_1_1	38934372	31.82122637	-103.9151443	0.41
NE_1_1	38933271	31.82747931	-103.9049179	0.78
NE_1_2_Average	N/A	**31.82631147**	**-103.9070584**	
NE_1_2	38934237	31.82457177	-103.9069582	0.19
NE_1_2	38934942	31.82931111	-103.9037861	0.45
NE_1_2	38934935	31.82505154	-103.9104309	0.35
NE_2_Average	N/A	**31.84990793**	**-103.8867983**	
NE_2	38934929	31.84629835	-103.8838846	0.49
NE_2	38935968	31.85351751	-103.889712	0.49
NE_3_Average	N/A	**31.89709799**	**-103.9629313**	
NE_3	38934661	31.89749479	-103.9627022	0.05
NE_3	38935357	31.89670119	-103.9631604	0.05
NE_4_Average	N/A	**31.93486384**	**-104.0183942**	
NE_4	38933299	31.92817853	-104.0107952	1.03
NE_4	38935108	31.94095599	-104.0108726	0.98
NE_4	38933620	31.94091722	-104.0262918	1.00
NE_4	38933298	31.92940362	-104.0256171	0.91
NE_5_Average	N/A	**31.87259943**	**-103.9486652**	
NE_5	38932872	31.87263544	-103.9438712	0.45
NE_5	38936030	31.86933526	-103.9477686	0.37
NE_5	38936032	31.87582758	-103.9543557	0.65
NE_6_Average	N/A	**31.91921509**	**-103.9596488**	
NE_6	38935886	31.92495056	-103.9593982	0.64
NE_6	38936478	31.91347962	-103.9598994	0.64
NE_7	38935373	**31.93565646**	**-103.9882531**	
NE_8_Average	N/A	**31.83066298**	**-103.9484245**	
NE_8	38932527	31.82703746	-103.9486369	0.40
NE_8	38932506	31.83053056	-103.9524	0.38
NE_8	38932507	31.83436782	-103.9485536	0.41

NE_8	38932528	31.83071608	-103.9441076	0.41
SW_1	10933058	**31.63327297**	**-104.0583867**	
SW_2	10932340	**31.6589148**	**-104.1202048**	
SW_3	10933071	**31.57716872**	**-104.126143**	
SW_4	38934925	**31.58041141**	**-104.0515104**	
SE_1_Average	N/A	**31.70387054**	**-103.8093091**	
SE_1	38934609	31.70808624	-103.8093091	0.47
SE_1	38935413	31.69965483	-103.8093091	0.47
SE_2_Average	N/A	**31.64368585**	**-103.8604012**	
SE_2	38933269	31.64410095	-103.8604012	0.05
SE_2	38936297	31.64327075	-103.8604012	0.05
SE_3	38935362	**31.632051**	**-103.9437564**	
NW_1_1	10932849	**31.74764785**	**-104.2234287**	
NW_1_2_Average	N/A	**31.74531493**	**-104.2486272**	
NW_1_2	10932848	31.7562617	-104.2543393	1.33
NW_1_2	10933282	31.74651467	-104.2404147	0.79
NW_1_2	10933281	31.73316843	-104.2511275	1.37
NW_2_Average	N/A	**31.86179886**	**-104.0906477**	
NW_2	10931638	31.86013189	-104.0867127	0.42
NW_2	10931565	31.86346583	-104.0945826	0.42

Table S6. Information of selected deep injection wells for the calculation. The well 10932704 in the last row, which was used in Tung et al. (2021), was not selected due to the long distance from the M5.0 event (~34 km). Instead, we chose the well 10933393 for the calculation. Nevertheless, ΔCFS caused by these two wells are relatively small: For 10932704, ΔCFS = 0.09 kPa, contributing to only 0.1% of the total ΔCFS in Tung et al. (2021); For 10933393, ΔCFS = -11 Pa in our calculation, indicating slip inhibition.

API	Injection depth (m)	Distance (km)	Latitude	Longitude	Total injection volume (BBLS)	ΔCFS (Pa)
10932395	4620	25.3	31.90386751	-104.1944243	30968068	95.26
10932532	4572	29.2	31.95741941	-104.1684945	31391720	-8.06
10932782	4510	18.1	31.81591015	-104.1945797	31218221	467.93
10932982	4804	11.3	31.78707537	-104.1291484	32822464	702.53
10933026	5030	16.7	31.86462427	-104.0764656	16452828	-87.35
10933166	5030	26.2	31.94728703	-104.1043423	19579260	-200.36
10933296	5180	20.9	31.9023804	-104.0804595	14439942	-159.57
10933393	4790	17.8	31.85911977	-104.13036601	4775928	-11.31
10932704	4420	34.1	31.94214235	-104.287393	6589535	

Table S7. Selected shallow injection wells for the sensitivity test. The pore pressure, normal stress, shear stress and ΔCFS listed here are simulation results based on geological model in Table 3.

Calculation groups	API number	Injection depth (m)	Pore pressure (Pa)	Normal stress (Pa)	Shear stress (Pa)	ΔCFS (Pa)
NW_1_1	10932849	1499.9	-242.3	1296.9	679.0	1311.8
NW_1_2	10932848	1493.5	15.5	856.2	504.4	1027.4
SE_1	38934609	2438.4	67.6	301.0	1760.2	1981.4
SE_2	38933269	1676.4	-195.0	-174.6	1470.7	1248.9
SW_1	10933058	1828.8	-2416.7	2107.9	1022.2	836.9
SW_2	10932340	1676.4	-1257.3	1375.2	605.0	675.8
NE_1_1	38934274	1783.1	-710.7	2867.3	1319.8	2613.8
NE_1_2	38934237	2304.3	-693.9	1717.8	695.0	1309.3
NE_1_2	38934942	2304.3	-183.6	1370.6	708.7	1420.8
NE_2	38934929	2304.3	153.1	1083.0	418.8	1160.4

Table S8. Results of sensitivity test. The pore pressure, shear and normal stresses, and total ΔCFS shown are the cumulative values from 10 shallow injection wells.

Parameters changed compared to geological model in Table 3	Total pore pressure (Pa)	Total normal stress (Pa)	Total shear stress (Pa)	Total ΔCFS (Pa)
Shale layer: ν_u = 0.47, B=0.94 (identical to the model in Tung et al. (2021))	-5479.74	12703.49	9134.75	13469.00
Shale layer: B=0.7	-5436.27	12754.56	9170.12	13561.10
Shale layer: B=0.8	-5412.86	12706.84	9156.83	13533.22
Shale layer: B=0.9	-5384.33	12663.07	9142.37	13509.61
Sandstone layer: D=0.1	3365.62	6624.91	11489.57	17483.89
Sandstone layer: D=0.5	-4339.12	12197.14	9757.51	14472.33
Sandstone layer: D=1.0	-6727.20	13097.33	8056.28	11878.36

Table S9. Seismic activity within 10 km of the mainshock ranges from 2017 to 2021 from the TexNet earthquake catalog.

Table S10. Information of selected shallow injection well (SI-1).

API	UIC number	Injection depth (m)	Latitude	Longitude	Total injection volume (BBLS)
38934237	000108878	2305	31.825	-103.90695815	30472454

Video S1. Temporal and spatial evolution of seismic activities within 10 km of the M5.0 Mentone earthquake from 2017 to 2021.

References

Sheng, Y., Pepin, K. S., & Ellsworth, W. L. (2022). On the depth of earthquakes in the Delaware Basin: A case study along the Reeves–Pecos county line, *Seismol. Rec.* **2,** no. 1, 29–37.

Tung, S., Zhai, G., & Shirzaei, M. (2021). Potential link between 2020 Mentone, West Texas M5 earthquake and nearby wastewater injection: implications for aquifer mechanical properties, *Geophys. Res. Lett.* **48,** no. 3, doi: 10.1029/2020GL090551.

Potential Poroelastic Triggering of the 2020 M5.0 Mentone Earthquake in the Delaware Basin, Texas, by Shallow Injection Wells

by Xinyu Tan* and Semechah K. Y. Lui*

Department of Chemical and Physical Sciences, University of Toronto Mississauga, 3359 Mississauga Road, Mississauga, Ontario, Canada, L5L 1C3, xy.tan@mail.utoronto.ca, semechah.lui@utoronto.ca (X.T., S.K.Y.L.)

Corresponding author: xy.tan@mail.utoronto.ca

*Also at Department of Earth Sciences, University of Toronto, 22 Russell Street, Toronto, Ontario, Canada, M5S 3B1.

KEY POINTS:

- The M5 Mentone event occurred on a south-facing normal fault with a strike and dip of 81 and 52 degrees.
- Shallow injections may have promoted the occurrence of the mainshock by poroelastic stress perturbations.
- Rock properties of the injection layer can notably affect coupled pore pressure and stress perturbations.

ABSTRACT

The Delaware Basin in Texas, one of the largest oil and gas production sites in the US, has been impacted by widespread seismicity in recent years. The M5.0 earthquake that occurred in March 2020 near the town of Mentone is one of the largest induced earthquakes recorded in this region. Characterizing the source parameters and triggering mechanism of this major event is imperative to assess and mitigate future hazard risk. A former study showed that this event may be attributed to the deep injection nearby. Interestingly, the earthquake is located in proximity to shallow injection wells with much larger total injection volume. In this study, we investigate the role of these shallow injection wells in the triggering of the M5.0 event despite their farther distance from the mainshock. We perform source-parameter inversion and earthquake relocation to determine the precise orientation of the south-facing normal fault plane where the mainshock occurred, followed by fully coupled poroelastic stress modeling of the change of Coulomb Failure Stress (ΔCFS) on the fitted fault plane caused by shallow injection in the region. Results show that shallow wells caused up to 20 kPa of ΔCFS near the mainshock location, dominated by positive poroelastic stress change. Such perturbation surpasses the general triggering threshold of faults that are well aligned with the local stress field and suggests the nonnegligible role of these shallow wells in the triggering of the mainshock. We also discuss the complex effect of poroelastic stress perturbation in the subsurface and highlight the importance of detailed geomechanical evaluation of the reservoir when developing relevant operational and safety policies.

INTRODUCTION

Underground fluid injection, such as hydraulic fracturing, wastewater disposal, geothermal utilization and carbon sequestration, has led to a dramatic increase of seismicity globally (Ellsworth, 2013; Bao & Eaton, 2016; Keranen & Weingarten, 2018). In the Delaware Basin, Texas, the increase of oil and gas related activities has resulted in widespread seismicity in recent years (Skoumal et al., 2020, 2021; Zhai et al., 2021). Between 2014 and 2018, 24 sizable earthquakes ($M \geq 3$) have occurred in the Basin, while only 20 were reported in the previous 25 years combined (1970 – 2014) (Skoumal et al., 2020). On March 26, 2020, a M5.0 event occurred near Mentone and close to the border of Reeves County and Culberson county, which is one of the largest induced earthquakes in Texas to date (Figure 1).

For induced events that occur on faults close to injection operations, their activation is typically attributed to the build-up of pore pressure from neighboring wells (Keranen et al., 2013), though it has also been suggested that pore fluid can diffuse over large distances and trigger earthquakes remotely (Keranen et al., 2014; Yeck et al., 2016). For the Mentone earthquake, there are only 4 shallow injection wells within 5 km, all with small cumulative injection volume ($< 6 \times 10^6$ BBLs). Wells with much larger volume are located at distances between 10 km and 25 km (Figure 1).

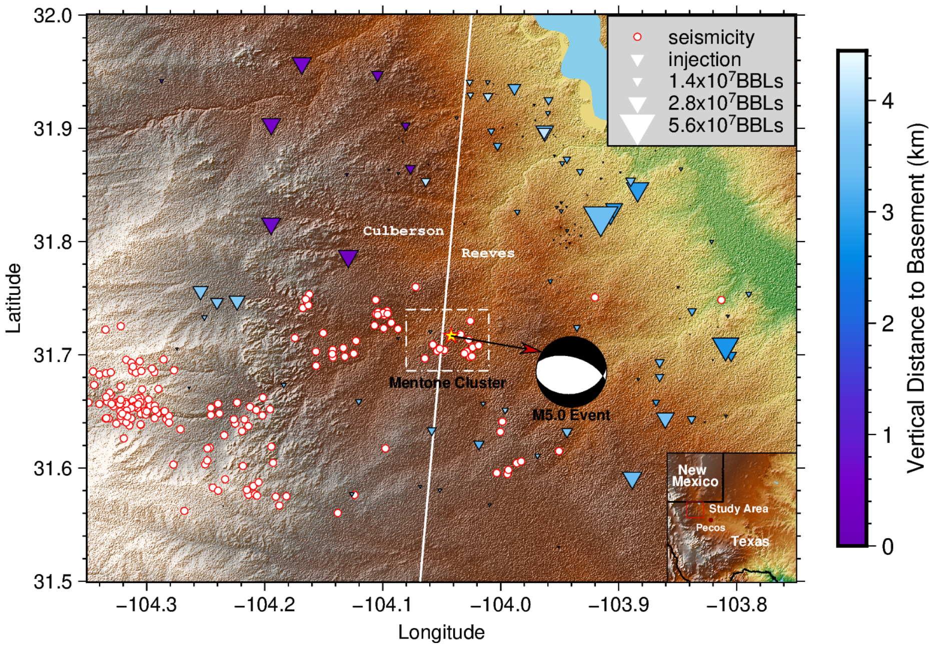

Figure 1. Location of injection wells (inverted triangles) and seismic events (red circles) within 25 km of the mainshock (yellow star). The size and color of the inverted triangles are proportional to the injection volume and the vertical distance between the injection wells and the basement, respectively. The Mentone (mainshock) cluster is enclosed in the white dashed rectangle. The bottom-right inset shows the location of the study area (red rectangle) in western Texas. Purple inverted triangles are deep injection wells included in the study by Tung et al. (2021).

Tung et al. (2021) attributed the cause of the M5.0 event to the fluid diffusion from deep injection wells in the highly permeable Ellenburger group (limestone layer) located to the northwest of the mainshock, assuming a hydraulic connection between the limestone layer and the basement. Interestingly, apart from these deep wells, there are also a lot of shallow injection wells within 25 km of the mainshock with much larger total injection volume, approximately five times larger than that of the deep wells (Figure 2). In particular, shallow wells to the northeast of the mainshock alone have contributed a volume 2.5 times larger than that of the deep injection wells, which is also the largest among the four quadrants around the mainshock. These shallow wells, despite their relatively large epicentral distance (> 5 km), may entertain the possibility of remote triggering due to their high injection volume (Goebel et al., 2017; Goebel & Brodsky, 2018; Zhai et al., 2021). Motivated by this, we investigate in this study the potential contribution of these shallow injection wells to the Mentone earthquake and the possible triggering mechanisms. We analyze their perturbations in pore pressure and coupled poroelastic stress caused on the reactivated basement fault without assuming any hydraulic connection in the reservoir.

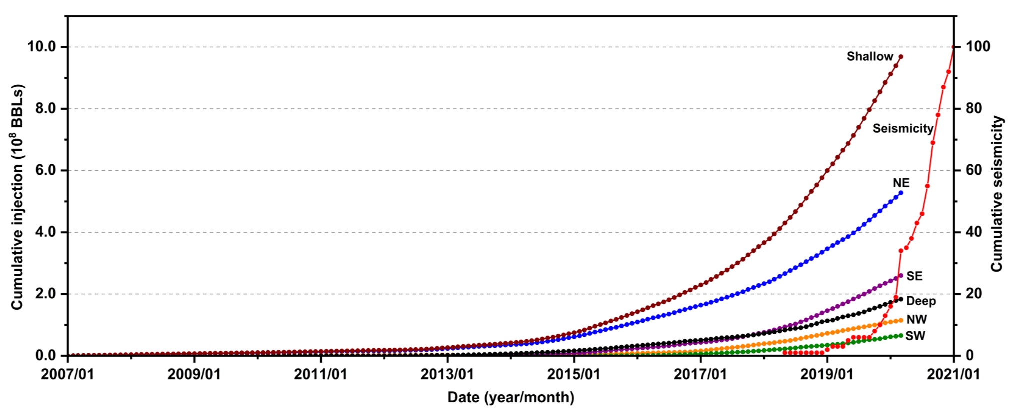

Figure 2. Cumulative seismicity within 25 km of the mainshock (red curve; up to January 2021) and injection volume of injection wells up to the occurrence of the Mentone event in March 2020. “Shallow” represents cumulative injection volume of all shallow wells within 25 km of the mainshock, and “Deep” represents deep injection wells used in Tung et al. (2021). “NE”, “NW”, “SW”, and “SE” represent individual cumulative injection volume of shallow wells in the northeast, northwest, southwest, and southeast quadrant, respectively.

Previous studies showed that the normal and shear stress on the fault plane are highly sensitive to the location and orientation of the fault (Deng et al., 2020; Lim et al., 2020), hence, correctly resolving the orientation of the fault plane is an imperative step. In this work, we first perform source parameter inversion on the mainshock and selected adjacent events considering their time and location proximity to the mainshock. Then we constrain the fault plane orientation by fitting relocated events. Lastly, we conduct fully-coupled poroelastic modeling to calculate the change of the Coulomb failure stress (ΔCFS) on the fitted fault plane and investigate the effects of shallow injection wells on the occurrence of the M5.0 event. In the following sections, we first introduce the methods and discuss the results on earthquake relocation and source parameter (focal mechanism, depth) inversion. Next, we detail the methods in conducting the poroelastic modeling and the analysis result. In the Discussion section, we further elaborate on the validation of triggering by shallow injection based on the spatiotemporal distribution of nearby seismicity, as well as the complexity in assessing the role of poroelastic triggering.

SOURCE PARAMETER INVERSION AND EARTHQUAKE RELOCATION

Data and Methods

To better constrain source parameters and identify events that potentially occurred on the mainshock fault plane, the Cut and Paste (CAP) method (Zhao & Helmberger, 1994) is utilized to perform the focal mechanism and depth inversion. Through fitting synthetic and observed waveforms of segmented body and surface waves, the CAP method is capable of resolving the optimal source mechanism by grid-searching the seismic moment (M_0), focal mechanism, and depth of the target event with minimum misfit. Here we use the frequency-wavenumber method to compute the Green's functions as 1D synthetic waveforms input for the inversion (Zhu & Rivera, 2002). The 1D velocity model used in our inversion is derived jointly from sonic velocity logs of a well in the Delaware Basin (Sheng et al., 2022) and the central United States velocity model (CUS). For details of the model, see Figure S1 in supplemental material to this article.

In terms of events selected for focal mechanism inversion, apart from the small cluster containing the mainshock (the Mentone cluster in Figure 1), there are also some neighboring events located between 5 and 10 km to the west and northwest of the mainshock. To determine whether these events occurred on the mainshock fault plane, we conducted focal mechanism inversion on seven events with $M \geq 3.0$, three of which from the Mentone cluster and the other four from the neighboring clusters (Table 1).

Table 1. Catalog information of selected events obtained from IRIS.

Event	Catalog time	Latitude	Longitude	Magnitude	Focal Depth (km)
01	2020-03-26 15:16:27	31.7168	-104.0419	5.0	9.51
02	2020-03-26 08:52:41	31.7065	-104.0237	3.8	5
03	2020-03-29 01:27:06	31.7029	-104.0288	3.5	5
04	2020-09-18 21:48:27	31.7061	-104.1334	3.5	5
05	2020-10-28 14:07:37	31.7011	-104.1244	3.7	5
06	2020-11-15 15:44:53	31.7349	-104.0986	3.3	5
07	2020-09-03 03:52:27	31.7360	-104.1057	3.0	8.03

Apart from using focal mechanism information to constrain the orientation of the mainshock fault plane, we also relocate earthquakes near the M5.0 event to minimize hypocenter uncertainty and to allow for individual fault structures to be delineated, which is conducive to subsequent stress and pressure calculation. While many wells within 25 km are to the northeast of the mainshock, most seismicity are located to the southwest end of the mainshock (Figure 1). Here we perform HypoDD relocation (Waldhauser & Ellsworth, 2000) on earthquakes with azimuths to the mainshock ranging between 225° and 325° , which include the Mentone cluster and two other clusters aforementioned (Figure 3). 41 stations with epicentral distance between 20 and 230 km are selected for the analysis (Table S1).

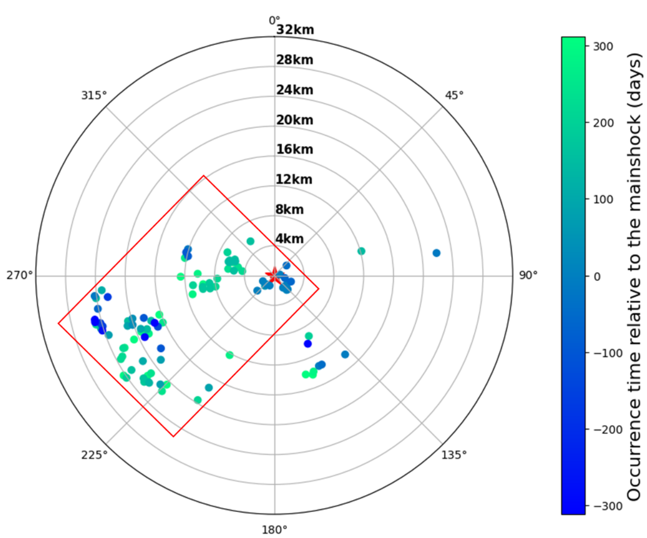

Figure 3. Radial plot displaying events located within 25 km from the mainshock (the red star). Selected events for hypoDD relocation are enclosed within the red rectangle. Colorbar indicates the relative occurrence time of earthquakes to the mainshock.

We first use PhaseNet (Zhu & Beroza, 2019) to generate phase arrival time automatically. Then, to better constrain the accuracy of relocation result, we calculate the cross correlation of data with

ObsPy's cross-correlation pick correction function following Deichmann & Fernandez (1992) and select data with correlations coefficient > 0.75 for hypoDD relocation. An example of phase pick output from PhaseNet and parameters used in HypoDD relocation are included in Figure S2 and Table S2, respectively. We also perform jackknife resampling to estimate the uncertainty (Table S3).

Results

The CAP inversion parameters and results are listed in Table 2. Resolved focal mechanisms (strike, dip, rake) of the M5.0 event are 288°, 51°, -67° and 74°, 44°, -115°, respectively, and the optimal focal depth is 6.6 km. Figure 4 shows the comparison between synthetic and observed waveforms of the M5.0 event at the optimal depth, the cross-correlation values of each waveform pair, and the relative misfit error at different focal depths. Inversion results of other selected events are in Figures S3 – S8. Based on similarity in focal mechanisms, events 01-07 likely belong to three different clusters: Cluster I include events 01 (mainshock), 02 and 03. Events 04 and 05 belong to cluster II, and events 06 and 07 to Cluster III. Events 04-07 likely occurred on fault planes different from the mainshock fault plane, considering their focal mechanism as well as relative time and location to the Mentone cluster.

Similar to focal mechanism inversion results, HypoDD relocation results also point to three separate earthquake clusters (Figure 5). Compared with catalog locations, relocated events within each cluster are positioned closer to one another. The orientations of the respective fault planes are approximated in 3D (Figure 6). The fitted strike/dip angles of clusters I, II and III are 81°/52°, 95°/58°, and 113°/73°, respectively. Although these three clusters share similar dip angles, there is obvious disparity among their strike angles and occurrence time relative to the mainshock. The fitted fault plane of cluster I shares similar strike and dip angles with the M5.0 mainshock and is regarded as the fault plane on which the earthquake occurred. We also applied the Jackknife method for the uncertainty estimation of the fault orientation of each cluster (Table S3). Overall, with 1000, 2000 and 3000 times of jackknife sampling, the standard deviation of the strike angle of fitted fault planes is smaller than that of the dip angle, which is reasonable with a generalized 1D velocity model. Besides, the relative standard deviation of the fitted fault plane I (~1% for strike and ~12% for dip angles) is the smallest among the three fitted fault planes (Strike/Dip = ~4%/~15% for fault plane II and ~9%/~25% for fault plane III). The results strengthen our confidence in using the fitted fault plane I as the mainshock fault plane to calculate the injection-induced fully coupled poroelastic perturbations.

Table 2. Parameters used in the CAP inversion and inverted focal mechanisms. Time windows for Pnl and S wave segments used in CAP are 35s and 70s, respectively.

Event	Filtered frequency range (Hz)		Focal Mechanism from CAP (strike, dip, rake)		Optimal depth (km)
	Pnl waves	S waves			
01	0.02-0.10	0.02-0.10	288°, 51°, -67°	74°, 44°, -115°	6.6
02	0.05-0.20	0.05-0.20	280°, 49°, -58°	56°, 50°, -121°	5.4
03	0.10-0.20	0.10-0.20	299°, 40°, -46°	67°, 62°, -120°	5.4
04	0.12-0.22	0.10-0.20	322°, 39°, -35°	80°, 68°, -123°	5.4

05	0.12-0.22	0.10-0.20	323°, 43°, -42°	86°, 62°, -124°	5.4
06	0.12-0.25	0.15-0.30	17°, 57°, -15°	115°, 77°, -146°	3.3
07	0.08-0.22	0.10-0.25	10°, 66°, -14°	105°, 77°, -155°	5.1

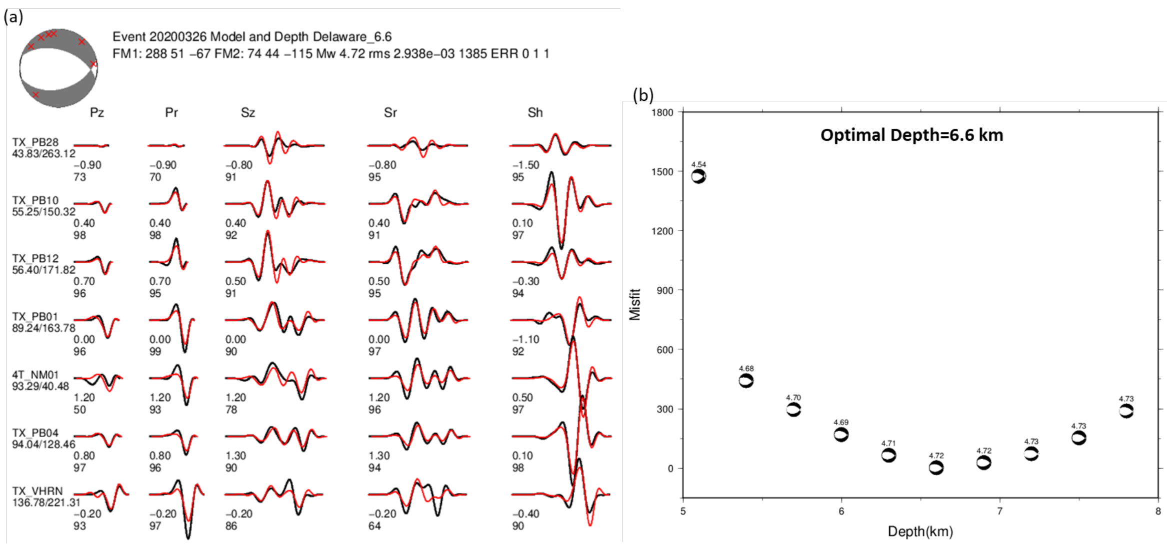

Figure 4. (a) Synthetic (red) and recorded (black) waveforms have the highest correlation at the optimal depth of 6.6 km for the M5.0 event. The numbers below the waveforms are optimal shift time (in second) and cross correlation coefficient, respectively. (b) Relative misfit error of the mainshock inversion at different focal depths. The number above each focal mechanism symbol is the best-fit event magnitude.

The mainshock depth after relocation (6.7 km) is considerably shallower than the IRIS catalog depth (9.51 km, Table 1), but is consistent with the centroid depth obtained from the independent CAP inversion (6.6km, Table 2) and from the TexNet earthquake catalog (7.1 km), which strengthens our confidence in the HypoDD relocation results. It should be noted that even though the 1D velocity model used for the source inversion may be simplified or imperfect, the CAP approach is capable of generating accurate source estimates because differential time shifts are allowed among the different body and surface waveform segments. Large shift in the focal depth after relocation is also shown in Sheng et al. (2022) for events in the neighboring region (Reeves-Peco County) and can be attributed to the sparse distribution of seismic stations and difference in the velocity model.

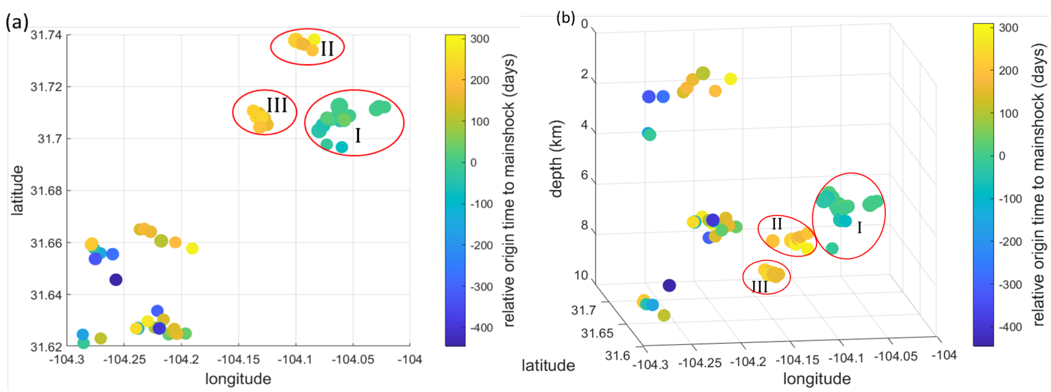

Figure 5. (a-b) 2D and 3D view of the relocated events, respectively. Colorbar represents their event time relative to that of the mainshock. Clusters I, II and III are circled in red.

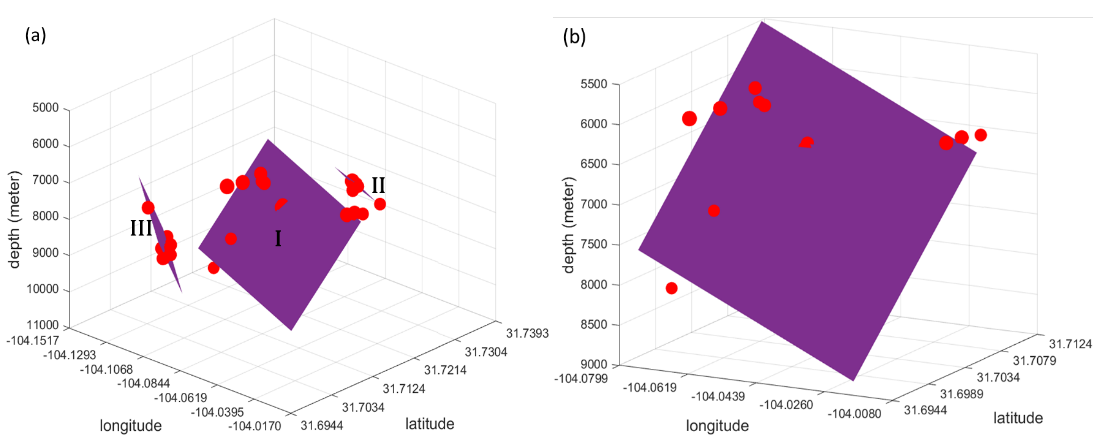

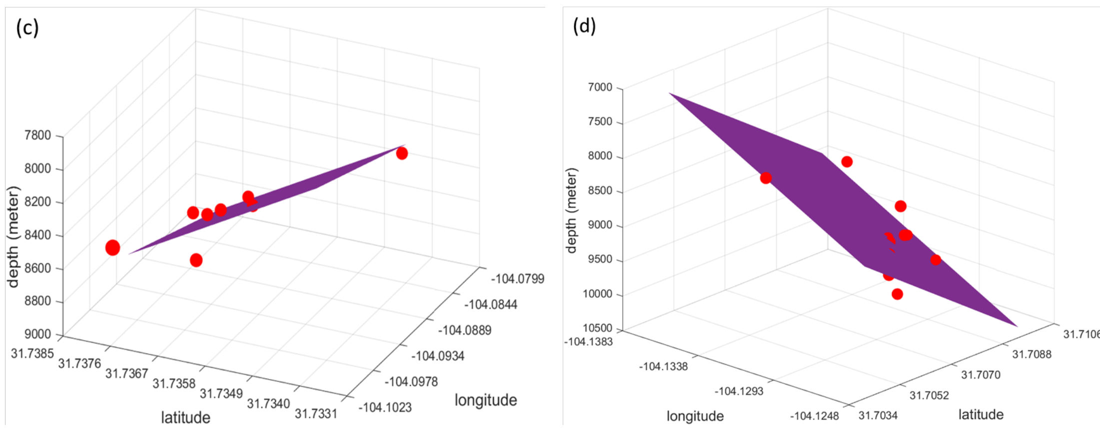

Figure 6. (a) Fitted fault planes of clusters I, II and III based on HypoDD results. (b)-(d) Zoomed-in plots of individual clusters I, II, and III, and their corresponding fitted planes.

FULLY-COUPLED MODELING OF POROELASTIC RESPONSE

Data and Method

With the relocated hypocenter and fitting fault plane, we compute the temporal change of pore pressure and poroealstic stress in the basement near the mainshock location due to shallow injections. We adopt the open-source package POEL (POroELastic diffusion and deformation), a semi-analytical method governed by the following equations (Wang & Kümpel, 2003):

$$(\lambda + 2\mu)\, \nabla\, (\nabla \cdot\, \mathbf{u}) - \mu\nabla\, \times (\nabla \times\, \mathbf{u}) - \alpha\nabla p = \mathbf{f}(\mathbf{x}, \mathrm{t}) \qquad (1)$$

$$Q^{-1}\frac{\partial p}{\partial t} + \alpha\frac{\partial}{\partial t}\nabla \cdot \mathbf{u} - \chi\, \nabla^2 p = q(\mathbf{x}, \mathrm{t}) \qquad (2)$$

Where λ and μ are the Lamé parameters, $\mathbf{u}$ is the displacement vector, α is the Biot's coefficient of effective stress, p is pore pressure, $\mathbf{f}(\mathbf{x}, \mathrm{t})$ is the body force on the rock matrix, Q^{-1} is bulk compressibility, χ is Darcy conductivity, and $q(\mathbf{x}, \mathrm{t})$ is the injection source. Both $\mathbf{f}(\mathbf{x}, \mathrm{t})$ and $q(\mathbf{x}, \mathrm{t})$ are functions of space ($\mathbf{x}$) and time (t). Equation (1) depicts the solid deformation coupled with the change of pore pressure due to fluid injection, which is the fluid-solid coupling. Equation (2) depicts the fluid mass conservation coupled from the solid deformation, which is the solid-fluid coupling (Chang & Segall, 2016; Zhai et al., 2021).

Through utilizing the analytical solution from Rudnicki (1986) for equation (1) and (2) in the homogeneous whole space, POEL models the pore pressure and strain tensor of rock matrix caused by time-varying injection in a cylindrically symmetrical layered poroelastic half-space (schematic illustration shown in Figure 7).

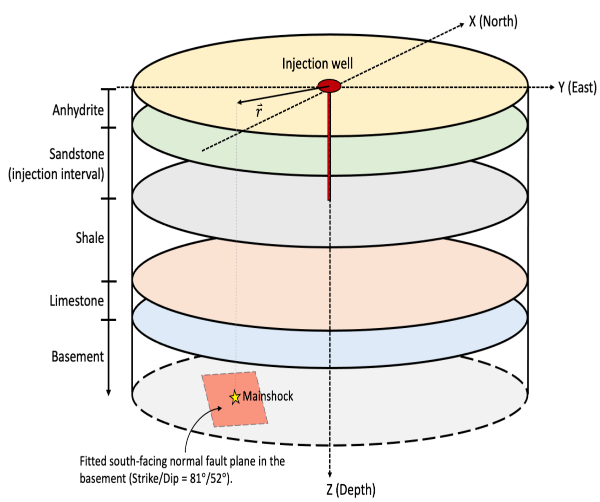

Figure 7. Schematic illustration of simulation domain in POEL (dimensions not to scale). Our model comprises of five geologic layers, with injection occurring within the sandstone layer. Coulomb failure stresses are calculated on the fitted fault plane near the mainshock hypocenter location.

In our simulation, boundary-value-problem mode is selected with an initial pore pressure of 0 MPa (Barbour et al., 2017). The input geomechanical parameters are shear modulus μ, Poisson's ratio ν of drained condition and ν_u of undrained condition, Skempton coefficient B and hydraulic diffusivity D. Other coupled poroelastic parameters, including λ, α, Q^{-1} and χ can be obtained with these five input parameters (Wang & Kümpel, 2003; Barbour et al., 2017):

$$\lambda = \frac{2\nu\mu}{1-2\nu} \tag{3}$$

$$\alpha = \frac{3(\nu_u-\nu)}{(1-2\nu)(1+\nu_u)B} \tag{4}$$

$$Q^{-1} = \frac{9}{2}\frac{(1-2\nu_u)(\nu_u-\nu)}{(1-2\nu)(1+\nu_u)^2\mu B^2} \tag{5}$$

$$\chi = \frac{9}{2}\frac{(1-\nu_u)(\nu_u-\nu)D}{(1-\nu)(1+\nu_u)^2\mu B^2} \tag{6}$$

We implement a geological model composed of five layers: (from top to bottom) anhydrite, sandstone, shale, limestone, and basement (Table 3; cf., Tung et al., 2021). All shallow and deep injections within 25 km from the mainshock occur in the high permeable sandstone and limestone layers, respectively (Figure S9 and Table S4). For geomechanical parameters, we apply those from Tung et al. (2021), except for D of the anhydrite/halite and shale layers, as well as ν_u and B of the shale layer, which are chosen from other relevant studies (Beauheim & Roberts, 2002; Makhnenko et al., 2011; Suarez-Rivera & Fjær, 2013; Li et al., 2020; Zhai et al., 2021). To this end, we also conduct a sensitivity study on the geomechanical parameters, which is detailed in the Results section below.

Based on results from POEL, we perform tensor transformation to obtain the local normal stress and shear stress on the fault plane where the mainshock occurred (Zoback, 2010) and analyze the Coulomb failure stress change (ΔCFS) on the fitted fault plane near the mainshock location. The Coulomb failure theory (Jaeger & Cook, 1979) states that ΔCFS is defined as:

$$\Delta\mathrm{CFS} = \Delta\tau + \mu(\Delta\sigma + \Delta p) \tag{7}$$

where $\Delta\tau$ and $\Delta\sigma$ represent the change of shear stress (positive for promoting failure) and normal stress (positive for unclamping the fault), Δp represents the change of pore pressure on the fault, and μ is the coefficient of friction. Fault failure is promoted when ΔCFS is positive, and vice versa. From equation (7), changes in direct pore pressure and the resulting poroelastic stress separately contribute to ΔCFS.

Table 3. Geological model used in our analysis.

Rock type	Depth (m)	μ (Pa)	ν	ν_u	B	D $(m^2 s^{-1})$
Anhydrite, halite	0 - 700	5.96E+09	0.26	0.40	0.86	0.00002
Sandstone	700 - 2500	26.91E+09	0.26	0.36	0.58	0.64000
Shale	2500 - 4500	26.91E+09	0.26	0.37	0.60	0.00002
Limestone	4500 - 5200	12.10E+09	0.26	0.36	0.65	1.00000
Basement	5200 -	30.86E+09	0.26	0.33	0.80	0.00002

For the poroelastic modeling, we select wells within 25 km of the mainshock with relatively large injection volume and divide them into four groups based on their locations from the mainshock, i.e. the northeast, southeast, southwest and northwest quadrants (Table S4). The selected wells account for 40-70% of the total injection volume in their respective quadrants. We compute their pressure and stress perturbation on the fitted fault plane separately and then combine their perturbations to obtain the overall contribution from all shallow injection wells. To simplify the calculation process, wells within each quadrant that are very close to one another are moved to an averaged location (Figure S10 and Table S5). Note that all the wells undergoing this simplification procedure are within 1.5 km from their average location. We examine the robustness of this averaging approach and confirm that the difference in pore pressure at the mainshock location caused by the simplification is minimal, i.e. ~5% of the total pore pressure perturbation. Wells at a farther distance apart are treated as individual wells at their true locations.

Results

The time evolution of the total monthly injection rate of selected wells, as well as the resulted change in pore pressure, normal stress, shear stress, poroelastic stress and ΔCFS are displayed in Figure 8. Detailed results of individual wells are listed in Table S4. It is found that at the early stage of the injection (before 2015) with low injection rate, pressure and stress perturbations near the mainshock are pretty small due to the large distance (10-20 km) between selected wells and the mainshock. Starting in 2015, with increasing injection rate, the total pore pressure perturbation near the mainshock transitioned from positive (encourage fault slip) to negative (inhibit fault slip), and the negative pore pressure increases with the injection rate. This phenomenon is mainly caused by the coupling effect of the poroelastic stress on the pore pressure. As the thick shale layer below the shallow injection sandstone layer has low permeability, direct pore pressure change due to percolation of injected fluid through the shale layer is unlikely. According to Chang & Segall (2016), injected fluid causes expansion of the layer below the injection layer, which subsequently compacts the layer at further distances. The boundary of expansion and compaction is determined by rock properties and injection parameters, and the zone of expansion gradually moves outward as injection continues. In the beginning, due to low injection rate and large distance between the injection wells and the mainshock, the basement rock layer near the mainshock location underwent compaction and, hence, the change in pore pressure remained positive until early 2018. As injection continued, the expansion region continued to move outward, and pore pressure eventually transitioned from positive to negative. Both normal and shear stresses increase throughout the entire injection period and they increase more rapidly with the rise of injection rate. The resulting poroelastic stress change reaches about 23 kPa at the time of the mainshock. Since the value of the pore pressure change at the mainshock location is negative, the positive ΔCFS was solely from poroelastic effects.

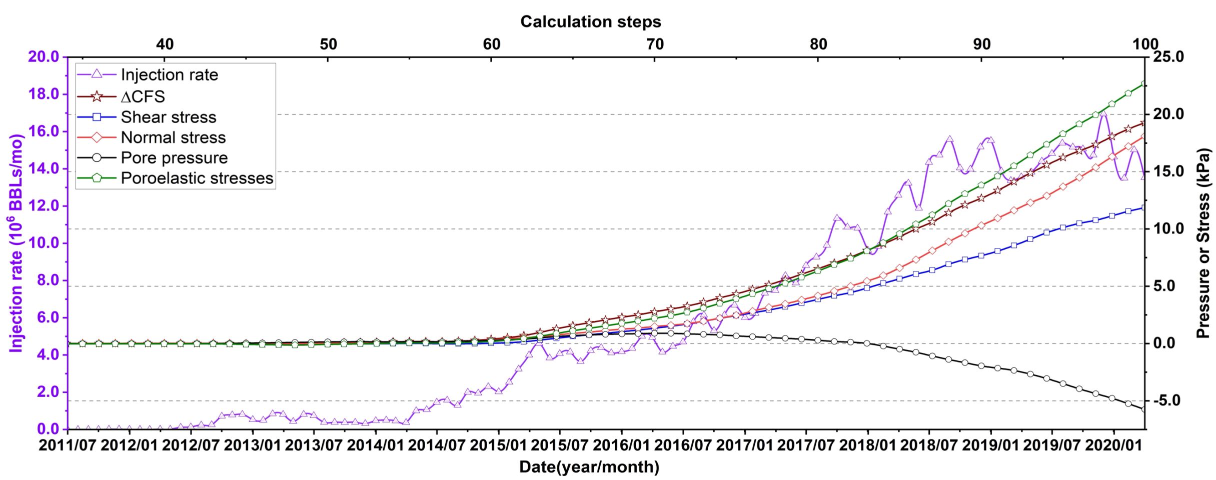

Figure 8. Time evolution of the monthly injection rate of selected shallow injection wells, as well as the change in pore pressure, poroelastic stress, normal stress, shear stress and ΔCFS on the fitted fault plane near the mainshock location until the occurrence of the M5.0 mainshock.

Overall, the ΔCFS increased with an increasing rate and reached ~20 kPa when the mainshock occurred, which surpasses the general threshold of 10 kPa for seismic events to be triggered (Rothert & Shapiro, 2007; Deng et al., 2020). Since the fitted fault plane is well aligned with the local stress field, it is possible that even a small perturbation may reactivate the fault (Lund Snee & Dvory, 2020). Furthermore, we only include wells with relatively large injection volumes in our calculation. If we account for the injection volume and location of all shallow wells, the total ΔCFS from shallow injection will be larger than 20 kPa. In Tung et al. (2021), it is suggested that the deep injection wells in the Ellenburger group (limestone layer) caused a ΔCFS of ~80 kPa near the mainshock location, assuming hydraulic connections between the limestone layer and the basement. For comparison, we calculate the pressure and stress perturbations of the deep injection wells to the northwest of the mainshock (Table S6 and Figure S11(a)), assuming no hydraulic connection. Results indicate that ΔCFS from deep injection wells would be reduced to ~1 kPa at the mainshock location, which is significantly smaller than the contribution from shallow injection wells in any of the four quadrants (Figure S11(b-e)). Therefore, our result implies that the shallow wells in this region can serve as the main driver of the M5.0 Mentone earthquake through poroelastic stress increase.

To test the robustness of our geological model, we also conduct sensitivity analysis on two geological parameters, namely the Skempton coefficient B of the shale layer ($B_{shale} = 0.7$, 0.8, and 0.9) and the hydraulic diffusivity D of the sandstone layer ($D_{Sandstone} = 0.1$, 0.5, and 1.0). In addition, we test a case with the Skempton coefficient B and the undrained Poisson's ratio v_u of the shale layer identical to those used in Tung et al. (2021). 10 of the shallow injection wells with larger ΔCFS contribution are selected for the analysis (Table S7). With the original set of parameters, these wells cause a cumulative ΔCFS of 13.5 kPa. In all the tested scenarios, the cumulative ΔCFS value ranges between 11.8 and 17.4 kPa, which remains larger than the general threshold of 10 kPa (Table S8). This strengthens our argument for the long-range poroelastic triggering from shallow injection wells.

DISCUSSION

Our work shares similar findings with earlier studies regarding the potential significant impact of shallow injection on deep geologic formations via poroelastic stress perturbations (Zhai et al., 2021). In fact, the spatiotemporal evolution of seismic activity near the M5.0 event may also shed lights on the triggering mechanism of events induced in the region. The TexNet earthquake catalogue showed that 330 seismic events were recorded within 10 km of the mainshock between 2017 and 2021, with $4.9 > M > 0.6$ (Table S9 and Video S1). A seismic swarm initially started to the northeast of the mainshock in late January 2020, then subsequent seismic events mostly occurred along a northeast-southwest-trending fault and exhibited a general migration pattern from northeast to southwest, with the mainshock among them in late March. Almost all the seismic events prior to the mainshock occurred at depths greater than 6 km, which may indicate the influence of the poroelastic stress perturbation from shallow injection. Besides, it is interesting to note that, within nine months after the M5.0 mainshock, there are two other seismic swarms that occurred to the west and northwest of the mainshock in the basement layer, with average depths > 6 km (clusters II and III in relocation analysis; Video S1). Their occurring after the mainshock and farther distance from the major shallow injection wells suggest that they may also be the result of poroelastic triggering due to shallow injection. Hence, we argue that the spatiotemporal distribution of nearby seismicity confirms the non-negligible role of the poroelastic stress perturbation in this region.

The effect of poroelastic stress in earthquake triggering can be challenging to assess and depends on multiple factors such as the subsurface structure and the injection history. To establish a more detailed comparison of the effects of subsurface hydrogeological properties, we model a shallow-injection scenario (called SI-2 hereafter) and compare that against the original shallow injection scenario (called SI-1 hereafter; Figure S12 and Table S10), with the sole focus on the properties of the injection layer. All parameters are kept constant except for the rock properties of the injection layer: Sandstone in SI-1 and limestone in SI-2. The resulted pore pressure change is smaller in the limestone layer (SI-2) than in the sandstone layer (SI-1) (Figure S13). The change in normal stress, shear stress and ΔCFS (Figure 9) near the mainshock location is also smaller in SI-2. While these modeling results are numerically resolved in a multilayer setting, one can also obtain good first-order approximations with the steady-state analytical solutions of injection-induced poroelastic deformation $\mathbf{u}\,(\mathbf{x},\ t)$ and pore pressure $p\,(\mathbf{x},\ t)$ in a homogeneous whole space, which are fundamental equations used in the POEL package (Rudnicki, 1986; Wang & Kümpel, 2003):

$$\mathbf{u}\,(\mathbf{x},\ t) = \frac{q_o(1+\nu_u)B}{24\pi(1-\nu_u)D}\frac{\mathbf{x}-\mathbf{x_s}}{R} \tag{8}$$

$$p\,(\mathbf{x},\ t) = \frac{q_o}{4\pi\chi}\frac{\mathbf{1}}{R} \tag{9}$$

where $\mathbf{x_s}$ is the position of the injection source, $R = |\mathbf{x} - \mathbf{x_s}|$ is the distance between the injection source and the mainshock, and q_o is a constant injection rate. According to these two equations, $\mathbf{u}$ and p primarily depend on properties of the rock medium. Since $\chi_{limestone}$ is larger than $\chi_{sandstone}$ (4.2×10^{-11} m^2/(Pa·s) vs 1.5×10^{-11} m^2/(Pa·s)), that explains the larger pore pressure change in sandstone (SI-1) than in limestone (SI-2), according to equation (9). In equation (8), the term $\left[\frac{(1+\nu_u)B}{(1-\nu_u)D}\right]$ for limestone and sandstone are 1.3812 s/m^2 and 1.9258 s/m^2, respectively, and hence the poroelastic deformation is expected to be larger in a sandstone medium. Since SI-1 and SI-2 differs only by the rock type of the injection layer, the overall deformation $\mathbf{u}\,(\mathbf{x},\ t)$ in the basement layer where the mainshock occurs (6.7 km) would also be larger in SI-1 (Figure S14).

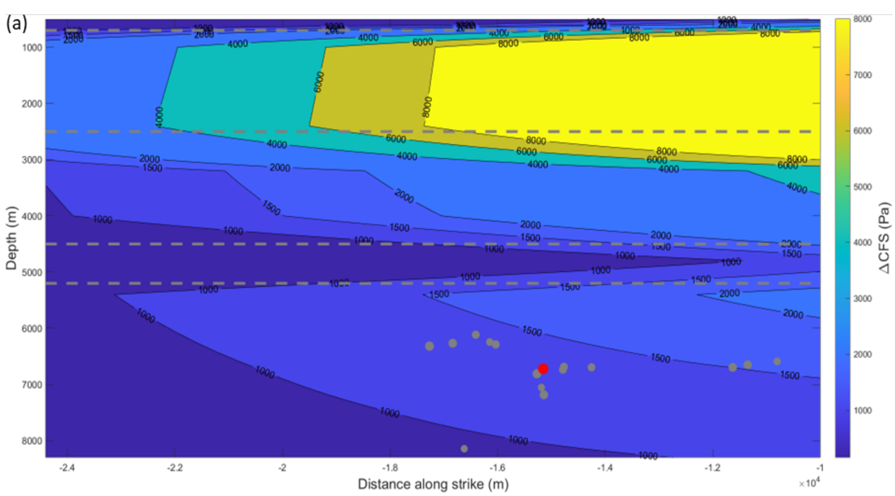

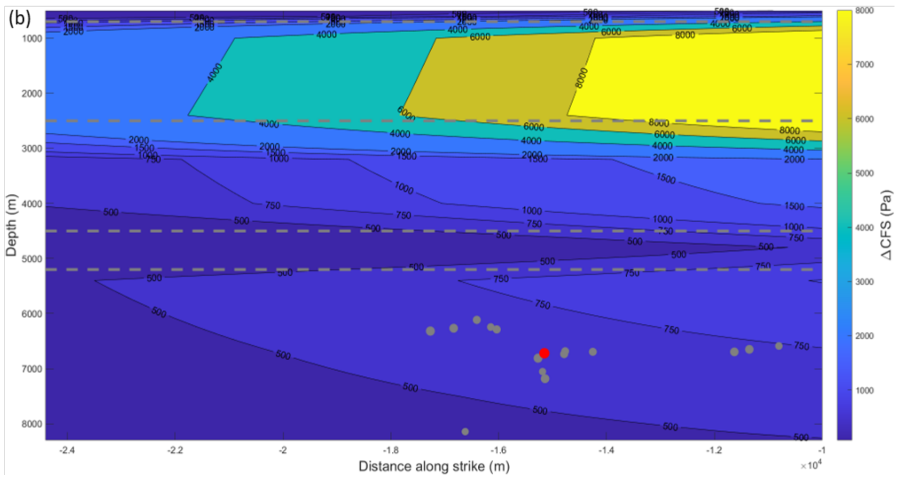

Figure 9. ΔCFS of injection scenarios (a) SI-1 and (b) SI-2. Gray dashed lines separate the anhydrite/halite, sandstone, shale, limestone and basement layers (from top to bottom). The red and grey circles denote the mainshock location and neighboring seismicity, respectively. Changes in pore pressure, normal and shear stress is shown in Figure S13.

At the mainshock depth of 6.7 km, injection in sandstone (SI-1) results in a much larger volumetric strain than in limestone (SI-2) for wells located within 20 km from the mainshock (Figure S15). Interestingly, volumetric strain decreases more slowly with distance in SI-2 (limestone), and hence the volumetric strain in SI-1 actually falls below that in SI-2 beyond 20 km. Furthermore, the volumetric strain in SI-1 becomes negative beyond 25 km. This can be explained by the injection-induced deformation transitioning from expansion to compression, and the exact position of this transition is, again, governed by the intrinsic rock properties, as well as the injection parameters (Chang & Segall, 2016).

Our modeling results demonstrate the essential roles that the hydrogeological properties of the injection layer and the distance between injection and preexisting fractures play in determining the extent of poroelastic deformation and ultimately the timing and location of induced seismicity. In the Delaware Basin, many shallow injection wells with large injection volume are located within 20 km of the mainshock, and hence our modeling results suggest that they can cumulatively cause significant poroelastic stress perturbations to the basement faults. In order to accurately assess the dominant mechanism controlling injection-induced seismicity and local and regional seismic risk, one would need clear imaging of subsurface structures, such as the hydrogeology of various rock layers and fault architecture that may act as hydraulic connections.

CONCLUSIONS

In this work, we perform source parameter analysis of the M5.0 Mentone earthquake in the Delaware basin and explore the potential role of shallow injection wells in the triggering of this earthquake. The M5.0 event occurred on a south-dipping normal fault in the basement at a depth of 6.7 km. Although the injection depth of these wells is far from the basement faults, due to their large injection volume, poroelastic stress perturbation contributes to significant cumulative ΔCFS of ~20 kPa. Depending on local fault architecture, our findings suggest that the shallow injection in the region may be the primary cause of the M5.0 earthquake. Our results confirm the significance of poroelastic stress triggering over large distances, especially when the injection volume is large. Furthermore, our study highlights the effect of rock properties of injection layers in the extent of pressure and stress perturbations caused by fluid injection. In this case, injection in sandstone results in much more prominent stress perturbations than in limestone. Overall, our results have important implications for future injection operations, especially when there exists thick impermeable geologic layers between the injection and basement faults. Due to the cumulative coupled poroelastic stress perturbation over large distances, regulators should consider the effects of fluid over an extensive region near injection sites when developing relevant operational policies.

DATA AND RESOURCES

Injection and seismic data are obtained from the Railroad Commission of Texas and Incorporated Research Institutions for Seismology (IRIS) Data Management Center, respectively (https://www.rrc.texas.gov/; last accessed January 2021; https://ds.iris.edu/wilber3/; with the following networks: (1) the TX (Texas Seismological Network; UT Austin, 2016); (2) the US (USNSN, Albuquerque, 1990); (3) the 4T (Texas Seismological Network; UT Austin, 2018); (4) the SC (New Mexico Tech Seismic Network; New Mexico Tech, 1999); (5) the GM (U.S. Geological Survey Networks; USGS, 2016). last accessed January 2021). Seismic event catalogue information is retrieved from and the United States Geological Survey (https://earthquake.usgs.gov/earthquakes/search/; last access January 2021). The TexNet Earthquake Catalog can be retrieved from https://www.beg.utexas.edu/texnet-cisr/texnet/earthquake-catalog. The injection data used in this study can be accessed through https://zenodo.org/record/7915695#.ZFpvlXaZOUk. The supplemental material includes figures and tables about relevant information and results of the CAP inversion and HypoDD relocation, schematic illustration and results of the injection-induced pore pressure and poroelastic calculation, and the sensitivity analysis based on the real injection history.

DECLARATION OF COMPETING INTERESTS

The authors declare that there is no competing interest existed in this article.

ACKNOWLEDGEMENTS

The authors would like to express their sincere thanks to Dr. Rongjiang Wang and Dr. Kai Deng for their helpful discussions. This work is supported by the Natural Sciences and Engineering Research Council of Canada (Discovery Grant 2019-06482). Sincere thanks are expressed to anonymous reviewers for the helpful suggestions to our manuscript.

REFERENCES

Bao, X., & Eaton, D. W. (2016). Fault activation by hydraulic fracturing in western Canada, *Science* **354,** no. 6318, 1406-1409.

Barbour, A. J., Norbeck, J. H., & Rubinstein, J. L. (2017). The effects of varying injection rates in Osage County, Oklahoma, on the 2016 M w 5.8 Pawnee earthquake, *Seismol. Res. Lett.* **88,** no. 4, 1040-1053.

Beauheim, R. L., & Roberts, R. M. (2002). Hydrology and hydraulic properties of a bedded evaporite formation, *J. Hydrol.* **259,** no. 1-4, 66-88.

Chang, K. W., & Segall, P. (2016). Injection-induced seismicity on basement faults including poroelastic stressing, *J. Geophys. Res.* **121,** no. 4, 2708-2726.

Deichmann, N., & Garcia-Fernandez, M. (1992). Rupture geometry from high-precision relative hypocentre locations of microearthquake clusters, *Geophys.J. Int.* **110,** no. 3, 501-517.

Deng, K., Liu, Y., & Chen, X. (2020). Correlation between poroelastic stress perturbation and multidisposal wells induced earthquake sequence in Cushing, Oklahoma, *Geophys. Res. Lett.* **47,** e2020GL089366, doi: 10.1029/2020GL089366.

Ellsworth, W. L. (2013). Injection-induced earthquakes, *Science* **341,** 1225942.

Goebel, T. H. W., Weingarten, M., Chen, X., Haffener, J., & Brodsky, E. E. (2017). The 2016 Mw5. 1 Fairview, Oklahoma earthquakes: Evidence for long-range poroelastic triggering at> 40 km from fluid disposal wells, *Earth Planet. Sci. Lett.* **472,** 50–61.

Goebel, T. H., & Brodsky, E. E. (2018). The spatial footprint of injection wells in a global compilation of induced earthquake sequences, *Science* **361**, 899-904.

Jaeger, J. C. & N. G. W. Cook (1979). *Fundamentals of Rock Mechanics, 3rd edition,* Chapman and Hall, London.

Keranen, K. M., Savage, H. M., Abers, G. A., & Cochran, E. S. (2013). Potentially induced earthquakes in Oklahoma, USA: Links between wastewater injection and the 2011 Mw 5.7 earthquake sequence, *Geology* **41,** no. 6, 699-702.

Keranen, K. M., Weingarten, M., Abers, G. A., Bekins, B. A., & Ge, S. (2014). Sharp increase in central Oklahoma seismicity since 2008 induced by massive wastewater injection, *Science* **345,** 448-451.

Keranen, K. M., & Weingarten, M. (2018). Induced seismicity, *Annu. Rev. Earth Planet. Sci.* **46,** 149–174.

Li, Z., Ripepi, N., & Chen, C. (2020). Using pressure pulse decay experiments and a novel multi-physics shale transport model to study the role of Klinkenberg effect and effective stress on the apparent permeability of shales, *J. Pet. Sci. Eng.* **189,** 107010.

Lim, H., Deng, K., Kim, Y. H., Ree, J. H., Song, T. R., & Kim, K. H. (2020). The 2017 Mw 5.5 Pohang earthquake, South Korea, and poroelastic stress changes associated with fluid injection, *J. Geophys. Res.* **125,** doi: 10.1029/2019jb019134.

Lund Snee, J. E., & Dvory, N. Z. (2020). Magnitude 5.0 earthquake shakes West Texas, *jenseriklundsnee. com.*

Makhnenko, R. Y., Riedel, J. J., & Labuz, J. F. (2011, June). Undrained plane strain compression of shale, in *45th US Rock Mechanics/Geomechanics Symposium*, OnePetro.

Rothert, E., & Shapiro, S. A. (2007). Statistics of fracture strength and fluid-induced microseismicity, *J. Geophys. Res.* **112.**

Rudnicki, J. W. (1986). Fluid mass sources and point forces in linear elastic diffusive solids, *Mech. Mater.* **5,** no. 4, 383-393.

Sheng, Y., Pepin, K. S., & Ellsworth, W. L. (2022). On the depth of earthquakes in the Delaware Basin: A case study along the Reeves–Pecos county line, *Seismol. Rec.* **2,** no. 1, 29–37.

Skoumal, R. J., Barbour, A. J., Brudzinski, M. R., Langenkamp, T., & Kaven, J. O. (2020). Induced seismicity in the Delaware basin, Texas, *J. Geophys. Res.* **125,** no. 1, doi: 10.1029/2019JB018558.

Skoumal, R. J., Kaven, J. O., Barbour, A. J., Wicks, C., Brudzinski, M. R., Cochran, E. S., & Rubinstein, J. L. (2021). The induced Mw 5.0 March 2020 west Texas seismic sequence, *J. Geophys. Res.* **126,** no. 1, e2020JB020693.

Suarez-Rivera, R., & Fjær, E. (2013). Evaluating the poroelastic effect on anisotropic, organic-rich, mudstone systems, *Rock Mech. Rock Eng.* **46,** no. 3, 569-580.

Tung, S., Zhai, G., & Shirzaei, M. (2021). Potential link between 2020 Mentone, West Texas M5 earthquake and nearby wastewater injection: implications for aquifer mechanical properties, *Geophys. Res. Lett.* **48,** no. 3, doi: 10.1029/2020GL090551.

Waldhauser, F., & Ellsworth, W. L. (2000). A double-difference earthquake location algorithm: Method and application to the northern Hayward fault, California, *Bull. Seismol. Soc. Am.* **90,** 1353–1368.

Wang, R., & Kümpel, H. J. (2003). Poroelasticity: Efficient modeling of strongly coupled, slow deformation processes in a multilayered half-space, *Geophysics*, **68,** 705-717.

Yeck, W. L., Weingarten, M., Benz, H. M., McNamara, D. E., Bergman, E. A., Herrmann, R. B., ... & Earle, P. S. (2016). Far-field pressurization likely caused one of the largest injection induced earthquakes by reactivating a large preexisting basement fault structure, *Geophys. Res. Lett.* **43,** no. 19, 10-198.

Zhai, G., Shirzaei, M., & Manga, M. (2021). Widespread deep seismicity in the Delaware Basin, Texas, is mainly driven by shallow wastewater injection, *Proc. Natl. Acad. Sci.* **118,** no. 20, doi: 10.1073/pnas.2102338118.

Zhao, L. S., & Helmberger, D. V. (1994). Source estimation from broadband regional seismograms, *Bull. Seismol. Soc. Am.* **84,** no. 1, 91-104.

Zhu, L., & Rivera, L. A. (2002). A note on the dynamic and static displacements from a point source in multilayered media, *Geophys. J. Int.* **148,** 619–627.

Zhu, W., & Beroza, G. C. (2019). PhaseNet: a deep-neural-network-based seismic arrival-time picking method, *Geophys. J. Int.* **216,** no 1, 261-273.

Zoback, M. D. (2010). *Reservoir geomechanics,* Cambridge university press, p. 156.